Biomass Conversion and Biorefinery (2026) 16:111
https://doi.org/10.1007/s13399-025-06946-2

ORIGINAL ARTICLE

Duckweed-derived magnetic adsorbent for efficient removal of methylene blue

Kelly Wong Kai Seng[1] · Alvin Lim Teik Zheng[2,3] · Karen Bulan Jeffrey[4] · Tan Toh Hii[5] · Eric Lim Teik Chung[6,7] · Jacqueline Lease[8] · Yoshito Andou[8,9]

Received: 11 January 2025 / Revised: 30 November 2025 / Accepted: 7 December 2025

Abstract

Low-cost and easily recoverable adsorbents are urgently needed for efficient treatment of dye-contaminated wastewater. In this study, a green magnetic duckweed-derived adsorbent (MDW) was synthesized via co-precipitation of Fe_3O_4 nanoparticles (NPs) onto dried duckweed using ascorbic acid (AA) as a reducing agent. The MDW exhibited a maximum methylene blue (MB) adsorption capacity of 78.59 mg/g under optimal conditions of pH 10, 50 mg/L initial MB concentration, 10 mg adsorbent dosage, and 60 min contact time, achieving a removal efficiency of 85.27%. Kinetic analysis showed that adsorption followed the pseudo-second-order (PSO) model ($R^2 > 0.999$), while equilibrium data were best described by the Temkin isotherm model, indicating heterogeneous surface interactions. Thermodynamic analysis revealed an exothermic and spontaneous process with negative $\Delta G°$ values across the temperature range of 298–318 K. The MDW retained over 69% of its initial removal efficiency after five regeneration cycles, confirming good reusability. Cost analysis estimated the synthesis cost at approximately RM 29.51/kg, highlighting economic feasibility. These findings demonstrate that MDW is a sustainable, low-cost, and magnetically recoverable adsorbent with strong potential for scalable wastewater treatment applications.

Highlights

- MDW achieved 78.59 mg/g MB adsorption capacity with easy retrieval using magnet.
- Retained over 69% efficiency after five regeneration cycle.
- MDW was produced at RM 29.51/kg using ascorbic acid as reducing agent.

Keywords Magnetic duckweed · Methylene blue · Wastewater treatment · Adsorption kinetics · Temkin isotherm · Low-cost adsorbent

✉ Alvin Lim Teik Zheng
alvinltz@upm.edu.my

1 Department of Agribusiness and Bioresource Economics, Faculty of Agriculture , Universiti Putra Malaysia, Serdang 43400, Malaysia

2 Institute of Ecoscience Borneo, Universiti Putra Malaysia Sarawak, Bintulu, Sarawak 97008, Malaysia

3 Department of Science and Technology, Faculty of Humanities, Management and Science, Universiti Putra Malaysia Sarawak, Bintulu, Sarawak 97008, Malaysia

4 Department of Chemistry, Faculty of Resource Science and Technology, Universiti Malaysia Sarawak, Kota Samarahan, Sarawak 94300, Malaysia

5 Department of Animal Science and Fisheries, Faculty of Agricultural and Forestry Sciences, Universiti Putra Malaysia Sarawak, Bintulu, Sarawak 97008, Malaysia

6 Department of Animal Science, Faculty of Agriculture, Universiti Putra Malaysia, Serdang 43400, Malaysia

7 Institute of Tropical Agriculture and Food Security, Universiti Putra Malaysia, Serdang 43400, Malaysia

8 Graduate School of Life Sciences and Systems Engineering, Kyushu Institute of Technology, Fukuoka 808-0196, Japan

9 Collaborative Research Centre for Green Materials on Environmental Technology, Kyushu Institute of Technology, Fukuoka 808-0196, Japan

1 Introduction

Water is an indispensable resource vital for sustaining life, supporting industrial activities, and maintaining ecological balance. However, the escalating contamination of water bodies—primarily due to industrial effluents—has emerged as a major environmental and public health challenge [1–4]. Rapid industrialization and population growth have substantially increased the discharge of pollutants into aquatic environments, resulting in significant ecological degradation and health risks. Among these pollutants, dye-laden wastewater is particularly concerning, with global annual discharges amounting to millions of tons. This effluent severely impacts aquatic ecosystems and poses long-term health threats to humans. Unfortunately, many conventional treatment methods fall short in meeting current efficiency and sustainability requirements.

Dyes are commonly categorized based on their ionic characteristics into anionic, cationic, and non-ionic types. Anionic dyes such as azo and reactive dyes contain negatively charged groups and are predominantly used in the textile and paper industries. Cationic dyes, including methylene blue (MB), rhodamine B, and crystal violet, carry a positive charge and are extensively applied in textile, leather, cosmetic, and pharmaceutical sectors. These synthetic dyes are characterized by their high chemical stability and resistance to biodegradation, rendering them persistent in the environment. Their discharge into aquatic systems reduces light penetration, inhibits photosynthesis, and leads to bioaccumulation in aquatic organisms, thus posing severe threats to ecosystem health and biodiversity [5–9].

Among these, MB stands out due to its widespread use and recalcitrant nature. It is frequently utilized in textile, leather, paper, and cosmetic industries owing to its high solubility and chemical stability. However, its resistance to natural degradation and its toxicity—even at low concentrations—make it particularly hazardous to aquatic life and human health [10, 11]. Exposure to MB has been associated with adverse effects such as serotonin toxicity and potential carcinogenicity at concentrations exceeding 5 mg/kg [12].

To mitigate dye pollution, various physicochemical and biological treatment methods have been explored, including chemical oxidation, coagulation-flocculation, membrane filtration, and biodegradation [13–24]. Among these, adsorption has gained prominence as a preferred treatment strategy due to its operational simplicity, cost-effectiveness, high removal efficiency, and minimal generation of secondary pollutants. A wide range of adsorbents—such as activated carbon, biochar (BC), and agricultural waste-derived materials have demonstrated excellent dye removal capabilities. Nevertheless, the practical application of these materials is often limited by high production costs, challenges in regeneration, and energy-intensive synthesis processes.

Adsorption has emerged as a preferred method for eliminating dyes like MB from contaminated water. Its simplicity, cost-effectiveness, and high efficiency compared to other techniques, such as advanced oxidation processes, have made it a focus of wastewater treatment research [25–31]. Recent studies have shown promising MB adsorption capacities using biomass-derived adsorbents; however, issues like cost, regeneration, and large-scale applicability persist, which this study aims to address. In previous studies, most adsorption-modified materials derived from biomass were synthesized through carbonization followed by chemical activation [32–34]. This approach is energy-intensive, involves a complex process, and presents challenges in recovering the BC post-adsorption. Notably, oat hull BC demonstrated a superior maximum adsorption capacity compared to pea hull BC, with capacities of 183.4 mg/g and 145.5 mg/g, respectively, and removal efficiencies of 97% and 91% [35]. BC derived from rice straw achieved over 90% removal efficiency of MB at an optimal pH of 7, while bamboo-derived BC exhibited an impressive adsorption capacity of 67.46 mg/g towards MB [36]. Nonetheless, despite these advancements, the high cost and environmental impact associated with certain adsorbents, such as chemically treated activated carbon, remain significant barriers to their widespread application [37–40].

Duckweed *(Lemna spp.*), a floating macrophyte from the Lemnaceae family, attracts interest as an adsorbent precursor due to its rapid growth, high biomass productivity, and adaptability to tropical freshwater systems. Although uncontrolled proliferation disrupts aquatic ecosystems by reducing light penetration and dissolved oxygen, its dense biomass provides a useful resource for wastewater treatment [41]. Duckweed is rich in cellulose, hemicellulose, lignin, and oxygen-containing functional groups, which promote interaction with cationic dyes such as MB, while its thin tissue structure and natural porosity improve surface contact. Prior investigations reported effective MB adsorption by *Lemna minor* [42–44], and our earlier work achieved an adsorption capacity of 73.53 mg/g following pseudo-second-order (PSO) kinetics [45]. Duckweed presents operational advantages because it grows rapidly under nutrient-rich conditions, requires no cultivation cost when sourced from eutrophic waters, and is routinely removed as waste during waterway management [46]. Its use therefore supports biomass recovery strategies by converting nuisance growth into a treatment material, positioning duckweed as a resource-efficient alternative to agricultural residues and commercial carbon adsorbents.

The most commonly used iron oxides include hematite (α-Fe_2O_3), magnetite (Fe_3O_4), and maghemite (γ-Fe_2O_3). These materials are particularly valued in wastewater treatment due to their magnetic properties, selectivity, reactivity, and biocompatibility [47, 48]. Among them, magnetite (Fe_3O_4) stands out for its versatility, with co-precipitation being a widely adopted method for its synthesis. This technique involves the precipitation of iron salts in an alkaline medium, yielding magnetite NPs in a simple, efficient, and cost-effective manner. Ascorbic acid (AA) has emerged as a pivotal reducing agent in the synthesis of metal NPs due to its electron-donating capacity, which facilitates the reduction of metal ions to their metallic state [49, 50]. Similarly, in the context of magnetite NP synthesis, AA plays a critical role by reducing iron precursors like $Fe(acac)_3$, enabling the formation of Fe_3O_4 NPs. This approach eliminates the need for additional capping agents, producing NPs with controlled sizes and high reproducibility [51]. Moreover, AA contributes to the reductive dissolution of iron oxides, further enhancing the efficiency and precision of the synthesis process.

An important consideration in practical wastewater treatment is the efficient recovery of the adsorbent after use. Traditional adsorbents often require complex filtration or centrifugation steps, which can be time-consuming and costly. The incorporation of magnetite (Fe_3O_4) into the adsorbent matrix addresses this issue by imparting magnetic properties, allowing for rapid and straightforward separation using an external magnetic field. This not only simplifies the recovery process but also enhances the reusability and operational feasibility of the adsorbent in large-scale applications [52, 53]. Despite extensive research on biomass-based adsorbents, most reported systems rely on carbonisation, chemical activation, or energy-intensive processing routes, which increase cost and limit scalability.

In this work, a different design strategy is adopted by integrating raw duckweed biomass with magnetite through a low-temperature co-precipitation route using AA as a benign reducing agent. This approach eliminates pyrolysis and toxic reagents while enabling magnetic recovery of the adsorbent after use. The study establishes MDW as a functional adsorbent through coupled evaluation of adsorption efficiency, kinetic behaviour, equilibrium modelling, and thermodynamic feasibility. A cost-based assessment is further included to evaluate economic plausibility, which is rarely addressed in comparable studies. By linking green synthesis, magnetic separability, and performance validation within a single framework, this work positions MDW as a deployable material rather than a laboratory-only concept for dye-contaminated wastewater treatment.

2 Materials and methods

2.1 Materials

All chemicals used in this study were of analytical grade. Methylene blue (MB) (dye content≥82%) was purchased from Sigma-Aldrich and used without further purification. A 100 mg/L MB stock solution was prepared by dissolving 0.1 g of MB in 1 L of distilled water (Milli-Q, 18.2 MΩ·cm). pH adjustments were carried out using 0.1 M hydrochloric acid (HCl, 37%, Merck-KGaA) and 0.1 M sodium hydroxide (NaOH, ≥98%, Merck-KGaA). Analytical grade iron sulfate heptahydrate ($FeSO_4 \cdot 7H_2O$, ≥99%) were obtained from Bendosen (Malaysia) and used for the synthesis of Fe_3O_4 NPs. Ascorbic acid (AA) ($C_6H_8O_6$, ≥99%) was used as a green reducing agent and was also sourced from Sigma-Aldrich. All working solutions were freshly prepared before use to ensure accuracy and reproducibility in experimental conditions.

2.2 Preparation of DW

Natural duckweed (*Lemna minor L.)* was sourced from a retention pond in Bintulu. After collection, it was rinsed thoroughly with tap water to eliminate solid impurities and subsequently air-dried under sunlight. The sample was then subjected to further drying in an electric oven at 80 °C for 24 h to ensure complete removal of moisture. Once dried, the DW was milled and sieved to obtain an average particle size of 2 mm. The selection of 2 mm particle size for the prepared DW was based on achieving a balance between sufficient surface area for adsorption and ease of handling/separation. Smaller particles (e.g., < 1 mm) tend to aggregate and are more difficult to recover magnetically or filter, while larger particles (> 2 mm) exhibit reduced surface area and slower adsorption kinetics. Therefore, 2 mm was selected as the optimum size for laboratory-scale testing to ensure good dispersion, stable recovery, and effective interaction with dye molecules. The processed material was stored in a sealed plastic container to prevent moisture reabsorption and preserve its quality for future use.

2.3 Preparation of MDW

Specifically, the co-precipitation method to synthesize Fe_3O_4 NPs was modified from previous reports [54, 55]. A 0.05 mol/L solution of ferrous sulfate (50 mL) was prepared and mixed with a 0.1 mol/L solution of KOH (100 mL). Subsequently, 5 g of the dried DW was added to the mixture, which was then stirred using a magnetic stirrer and heated to 70 °C. Upon reaching 70 °C, a 0.05 mol/L solution of AA (30 mL) was added dropwise to the mixture. The mixture was continuously stirred for 2 h. Following this, the mixture was washed with distilled water and ethanol. The synthesized samples were collected using a centrifuge and dried in an oven at 60 °C for 24 h. The dried DW, denoted as magnetic duckweed (MDW), were then ground and stored for further analysis. The preparation steps of MDW are depicted in Fig. 1. The synthesis of MDW yielded approximately 2.34 g of MDW per 1.0 g of dried duckweed biomass, representing a 134% conversion efficiency.

2.4 Characterization

The point of zero charge (pHz) of the MDW was determined using previously reported method [56]. X-ray diffraction (XRD) patterns were obtained using a MiniFlex 600 diffractometer (Rigaku, Japan) with measurements were carried out using Cu-Kα radiation (λ = 1.5406 Å) Cu K-α radiation with a scan range of 10° to 80° (2θ) and a step size of 0.02°. The obtained data were processed with X'Pert Highscore Plus software. FTIR spectra were recorded using a Nicolet iS5 spectrophotometer (ThermoFisher Scientific, Japan) in the range of 4000 cm^{-1} to 500 cm^{-1} using KBr pellet method. The morphology of MDW was analyzed using a JCM-6000 Scanning Electron Microscope (JEOL Ltd., Japan).

2.5 Adsorption test

Batch adsorption experiments were conducted to evaluate the removal efficiency of MB using the synthesized MDW. Unless otherwise stated, all experiments were carried out at room temperature (25 ± 1 °C). A fixed dosage of 10 mg of MDW was added to 50 mL of MB solution with an initial dye concentration of 50 mg/L in a 100 mL Erlenmeyer flask. The solution was agitated at 150 rpm using a rotary orbital shaker Orbital Shaker, SHK-O0710, Infitek, China). The pH of the solution was adjusted to desired values (ranging from pH 3 to pH 10) using 0.1 M HCl or 0.1 M NaOH, and measured using a digital pH meter (Hanna Instruments, USA). Contact time was varied from 0 to 180 min to study adsorption kinetics, while temperature was controlled at 25 °C, 35 °C, and 45 °C for thermodynamic evaluation. Samples were withdrawn at predetermined time intervals, filtered, and analyzed using a UV–Vis spectrophotometer (IKEMELAB UV1200 UV-Vis, China) at λ_max = 664 nm to determine the residual MB concentration. The adsorption capacity (Q_e) of the MDW adsorbent was calculated using the following equation:

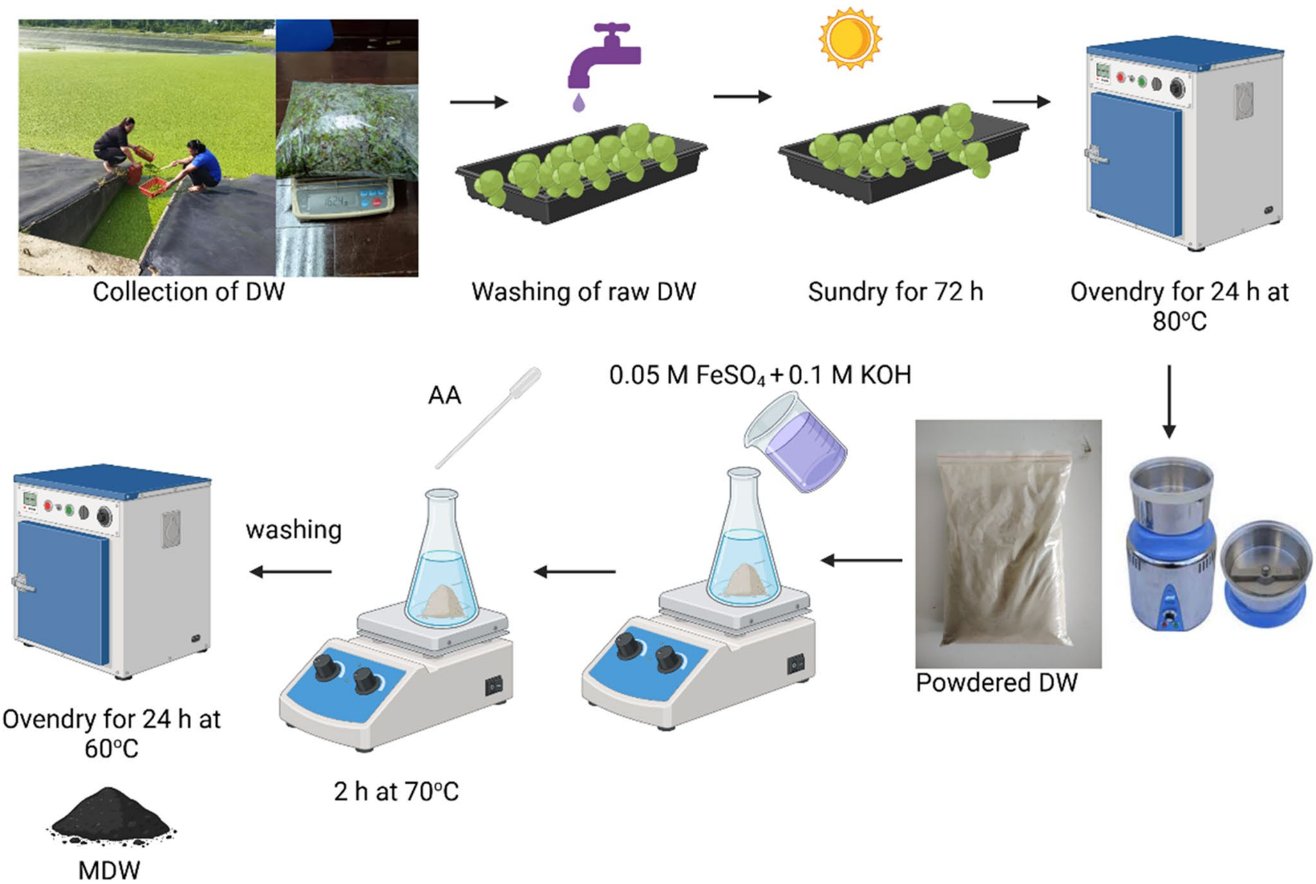

Fig. 1 Preparation steps of MDW

$$Q_e = \left(\frac{C_0 - C_e}{m}\right) V$$

The percentage removal efficiency was calculated using the following equation:

$$\%\, removal = \left(\frac{C_0 - C_e}{C_0}\right) \times 100$$

where C_0 represents the initial concentration (mg/g), C_t represents the equilibrium concentration at the specific time (mg/g), V is the volume of the dye solution (L) and m is the mass of the adsorbent (mg). The kinetic, isotherm, and thermodynamic studies were conducted in accordance with the methodologies previously outlined in our study [45]. Further details of the kinetic, isotherm and thermodynamic model equations, fitting parameters, and associated calculations can be found in the Supplementary Materials. Briefly, for the kinetic analysis, the adsorption data were evaluated using common models such as psuedo-first-order (PFO) and psuedo-second-order (PSO) and Elovich kinetic models to understand the rate of adsorption and the controlling mechanisms, whether physical or chemical [57, 58]. The isotherm studies aimed to determine the relationship between the adsorbate concentration and the amount adsorbed at equilibrium. Models such as Langmuir, Freundlich and Temkin isotherms were applied to the experimental data to analyze the adsorption capacity and surface interaction characteristics of the MDW. The thermodynamic parameters, including Gibbs free energy (ΔG), enthalpy (ΔH), and entropy (ΔS), were calculated to assess the spontaneity, feasibility, and energy changes associated with the adsorption process.

3 Results and discussion

This section presents an integrated analysis of the synthesis, characterization, and performance of the MDW. The results include material characterization (XRD, FTIR, SEM), batch adsorption under varied physicochemical conditions, kinetic and isotherm modeling, thermodynamic evaluation, regeneration studies, and cost analysis. Each subsection provides detailed insights into the functional behavior and applicability of MDW for MB removal in wastewater systems.

The SEM micrograph in Fig. 2(a) illustrates the morphology of magnetite synthesized via the co-precipitation method using ascorbic acid (AA) as the reducing agent. The resulting magnetite exhibits a granular structure composed of irregularly shaped and agglomerated particles, characterized by fractured surfaces and sharp edges. Particle clustering is evident, suggesting a natural tendency of magnetite NPs to aggregate due to magnetic dipole-dipole interactions [59]. Previously, we have reported on the SEM image of raw DW that reveals a complex and heterogeneous surface topology, displaying features such as cellular outlines, ridges, grooves, and protrusions [45]. After magnetite deposition, SEM images of MDW shown in Fig. 2(b) show that Fe_3O_4 NPs are well-dispersed across the DW surface, forming a relatively uniform coating with minimal large-scale aggregation. The surface retains its irregular porosity and rough morphology, indicating the preservation of micro- and mesoporous structures essential for adsorption. These structural modifications are subtle and mainly influence surface chemistry and magnetic properties rather than causing significant morphological changes. The surface characteristics of MDW align with previous studies on magnetic BC derived from plant waste, where partial pore

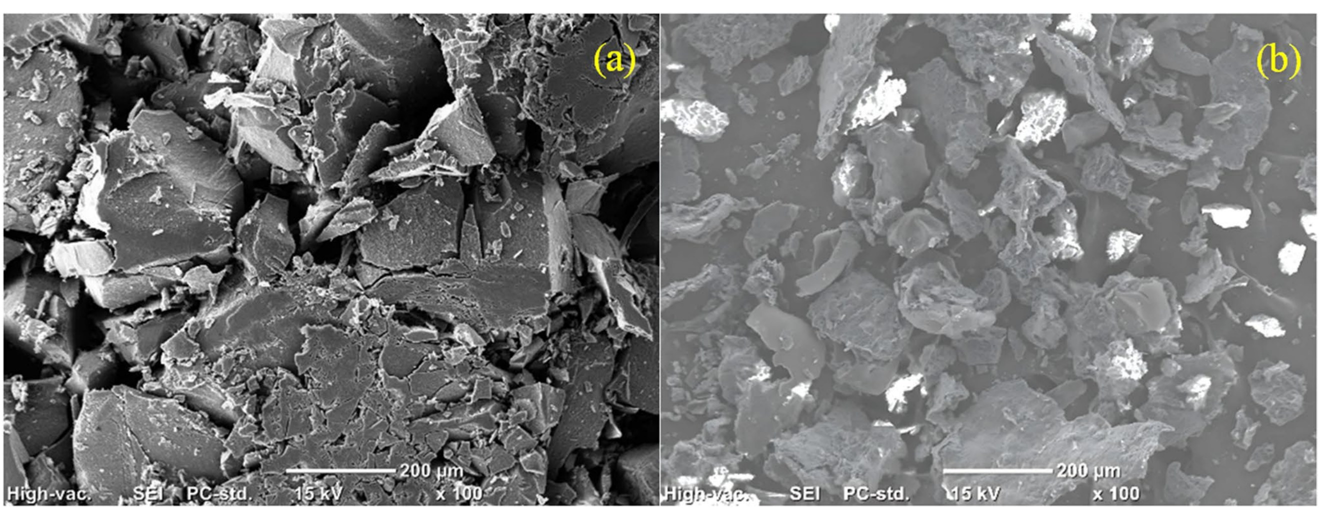

Fig. 2 SEM micrograph of (**a**) magnetite (**b**) MDW

blockage and NP clustering were also observed [60]. The heterogeneous yet consistent distribution of Fe_3O_4 ensures the availability of active adsorption sites. Furthermore, the morphology reveals a composite structure with both fine and coarse agglomerates, indicating successful integration of magnetite with the DW-derived matrix [61–63]. The presence of varied particle sizes and textures suggests that magnetite NPs are either anchored onto or embedded within the porous DW surface. A rough, layered texture with visible voids and pores is apparent, which could contribute to an increased surface area and enhanced adsorption capacity. Larger flakes and fibrous structures are attributed to the DW material, while denser, finer regions correspond to the magnetite NPs [64–66].

The XRD pattern of magnetite (red spectrum) shows sharp and well-defined peaks that correspond to the crystalline planes of magnetite (Fe_3O_4), as indexed by the JCPDS card number 19–0629 as shown in Fig. 3. Key diffraction peaks are observed at 2θ values near 30.1°, 35.5°, 43.2°, 53.5°, 57.1°, and 62.7°, which are indexed to the (220), (311), (400), (422), (511), and (440) planes of magnetite, respectively [67]. The high intensity and sharpness of these peaks confirm the crystalline nature of the synthesized magnetite. Additionally, minor peaks observed in the pattern do not correspond to the hematite (α-Fe_2O_3) phase, suggesting that the reduction conditions primarily favored the formation of magnetite, likely due to the mild reducing environment provided by AA [68]. The crystallite size was estimated using Scherrer's equation, with the (311) plane as the primary reference. The calculated crystallite size of approximately 9.23 nm indicates that the particles are in the nanometer range. Comparatively, studies that employed high-temperature treatments or alternative reducing agents reported mixed phases of Fe_3O_4 and α- Fe_2O_3, or even amorphous structures, highlighting the effectiveness of AA in promoting a well-defined Fe_3O_4 phase [69]. To further verify the formation of Fe_3O_4 in the inverse spinel structure, the lattice constant (a) was determined using Bragg's Law in conjunction with the cubic lattice equation. The calculation was based on the XRD diffraction angles corresponding to the characteristic (220), (311), and (400) planes, typical of Fe_3O_4. The resulting lattice parameter was calculated to be 8.38 Å [70]. The XRD pattern of MDW shows combined features from magnetite and duckweed-derived carbon. Characteristic reflections of magnetite remain detectable, yet their reduced intensity and peak broadening indicate lower crystallinity compared with pure Fe_3O_4. This change arises from interaction between magnetite NPs and the duckweed matrix, which restricts crystal growth and induces partial encapsulation within the carbon framework. The observed peak broadening further suggests nanoscale dispersion of Fe_3O_4, confirming successful integration of the magnetic phase into the biomass-derived structure. The broad peak observed in the XRD pattern of the MDW around $2\theta = 23°$ is characteristic of amorphous or disordered carbon [71]. It corresponds to the (002) plane of graphitic carbon but lacks the sharpness and intensity of crystalline graphite peaks, indicating a highly disordered structure. This amorphous feature suggests that the DW matrix contributes to the overall structure by forming a disordered, porous framework around the magnetite particles.

The FTIR spectra of pristine magnetite and MDW synthesized using AA are presented in Fig. 4. The FTIR spectrum of magnetite exhibits characteristic vibrational bands associated with its molecular structure. Magnetite prominent absorption peak observed at approximately 580 cm^{-1} ascribed to the Fe–O stretching vibrations, indicative of the spinel ferrite structure of magnetite [72, 73]. Additionally, a broad band in the 3400–3200 cm^{-1} region is attributed to O–H stretching vibrations from adsorbed water

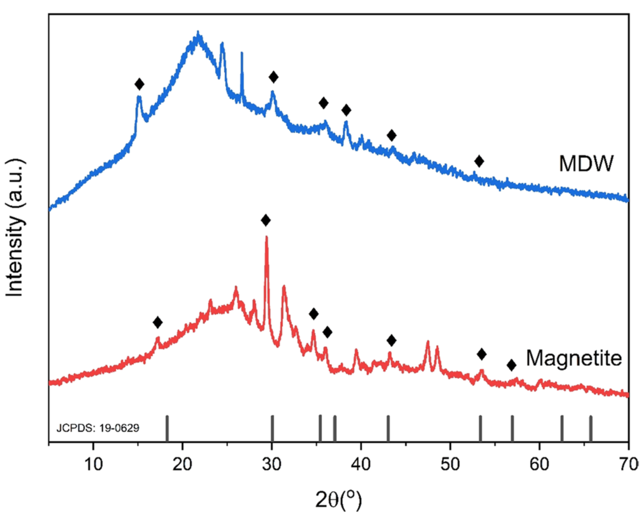

Fig. 3 XRD spectrum of magnetite and MDW

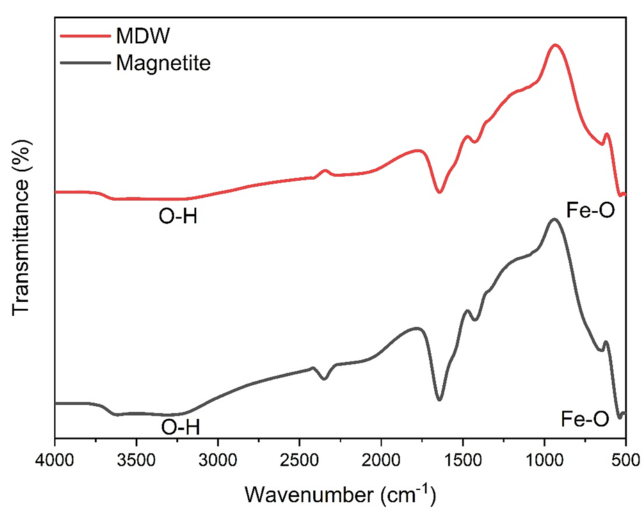

Fig. 4 FTIR spectrum of the MDW

molecules and surface hydroxyl groups [74, 75]. The FTIR spectrum of MDW retains the Fe–O band near 580 cm⁻¹, although it appears broader and less intense than in pure magnetite, suggesting strong interactions between Fe_3O_4 NPs and DW. The O–H band also broadens, indicating an increased presence of hydroxyl groups, likely introduced by functional constituents of the DW matrix, such as phenolics, proteins, and polysaccharides [76]. In addition to Fe–O and O–H bands, the MDW spectrum exhibits a peak near 1700 cm⁻¹, attributed to C=O stretching vibrations, and a weak band at ~1620 cm⁻¹, assigned to H–O–H bending of surface-adsorbed water. As reported previously for many plant materials, typically observed 1500–1600 cm⁻¹ for aromatic C=C stretching) is not clearly visible, possibly due to overlapping with the H–O–H bending. Notably, significant spectral shifts are observed in the 1400–1050 cm⁻¹ range, corresponding to C–O stretching of carboxyl and phenolic groups. These shifts suggest strong interactions likely coordination bonding or electrostatic linkages between Fe_3O_4 and the oxygen-containing functional groups of the contained in the DW [77]. These spectral changes confirm that Fe_3O_4 is chemically integrated into the MDW matrix rather than merely adsorbed, enhancing its structural stability and adsorption efficiency. The appearance of additional weak bands between 1200 and 1000 cm⁻¹ further confirms the presence of organic C–O functional groups from duckweed-derived materials. These groups, including hydroxyl (-OH), carboxyl (-COOH), and phenolic moieties, serve as active adsorption sites. The absence of new functional group peaks in the MDW spectrum can be attributed to the nature of the synthesis process and the interaction between Fe_3O_4 NPs and duckweed-derived carbon materials rather than the formation of new chemical bonds. The chemical functionalities present in the MDW may facilitate electrostatic interactions with the aromatic amine (-NH_2) groups of MB, dipole–dipole forces, and π–π stacking with MB molecules.

As shown in Fig. 5(a), the adsorption capacity (Q_e) of both adsorbents was observed to increase rapidly within the first 30 min of contact time. However, the rate of adsorption subsequently slowed down, indicating that the adsorption equilibrium was approached [78]. This phenomenon can be attributed to the abundance of active sites at the initial stage of adsorption, where negatively charged surface groups on DW such as oxygen-containing groups, carbonyls, alcohols, phenols, ethers, and esters that interacted with the positively charged MB [79, 80]. The rapid adsorption

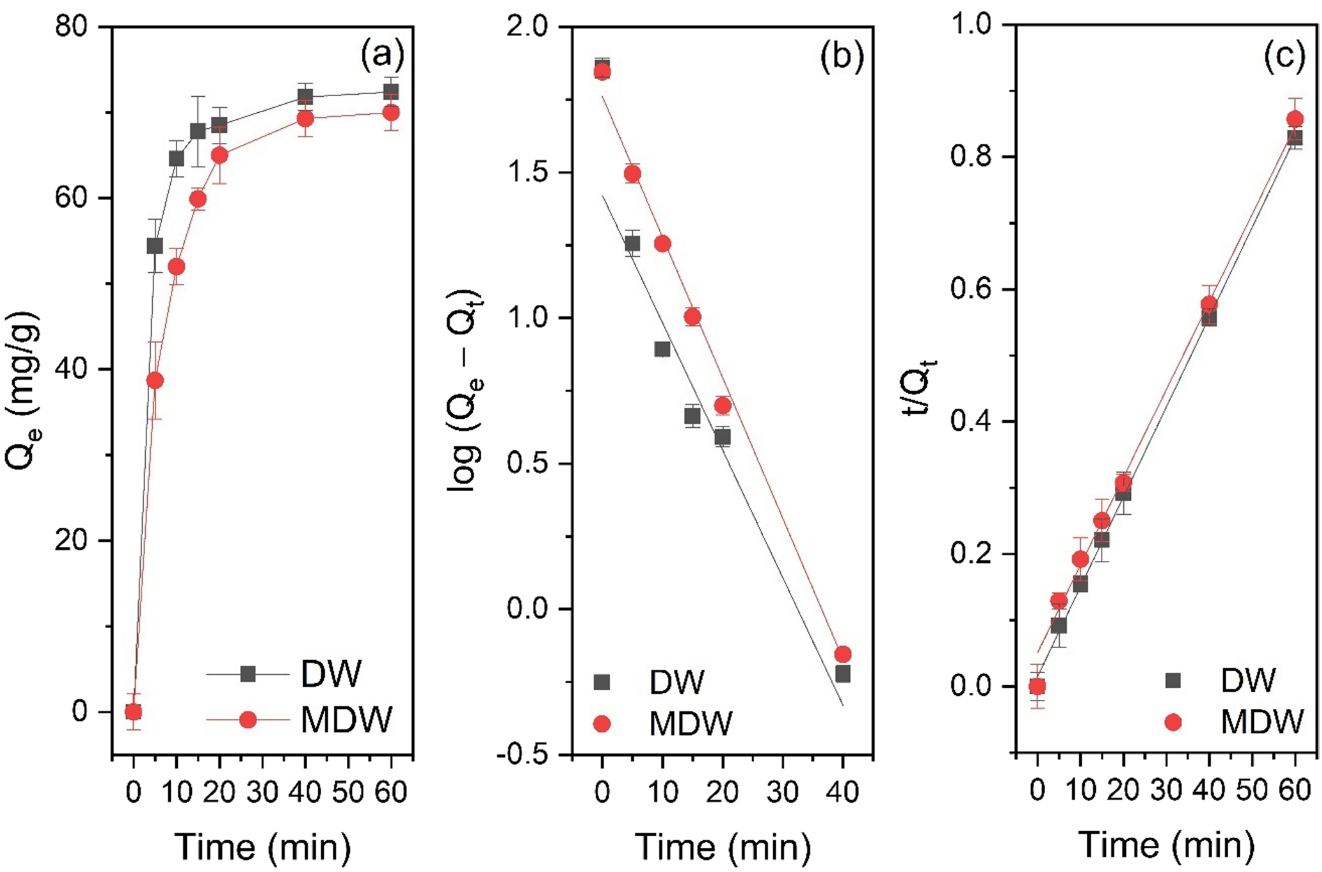

Fig. 5 (**a**) Adsorption capacity (**b**) PFO model and (**c**) PSO model for MB (10 mg/L) adsorption onto DW and MDW. Experimental conditions: Adsorbent dosage = 10 mg, Initial MB concentration = 10 mg/L, pH = 7, Temperature = 25 °C

phase was subsequently followed by a slower phase, caused by the saturation of the adsorbent sites and the electrostatic repulsion between the positively charged adsorbed species, which ultimately reduced the adsorption rate. DW exhibited a slightly higher adsorption capacity (72.4 mg/g) compared to DW (70 mg/g) after 60 min contact time. Although the adsorption capacity of MDW may be slightly diminished, their ease of separation through magnetic fields offers a significant advantage in practical applications, and subsequently analyzed for the adsorption behaviour under various parameters. The introduction of Fe_3O_4 NPs onto the DW may reduce the available active adsorption sites by partially blocking the pores responsible for dye uptake. DW primarily relies on electrostatic attraction and π-π interactions, where negatively charged surface functional groups bind efficiently to cationic MB molecules [45]. In MDW, the Fe_3O_4 modification enhances magnetic separation but modifies the surface charge distribution, affecting the electrostatic interactions.

To further analyze the adsorption kinetics, the data was fitted to the PFO and PSO models as depicted in Fig. 5(b) and Fig. 5(c), respectively. The linear plots obtained for the PSO model suggest that this model provides a better fit to the experimental data. The calculated correlation coefficients (R^2) for the PSO model were higher than those for the PFO, supporting its applicability. The closeness of the regression coefficient (R^2) to unity (1) indicates how well the calculation model fits the experimental data. The findings suggest that the adsorption of MB onto both DW and MDW is accurately described by the PSO kinetic model, which incorporates multiple diffusion steps. The parameters determined using PFO and PSO models are presented in Table 1.

Figure 6(a) illustrates the removal rate of MB from aqueous solutions using MDW. The experiment was conducted with three different masses of MDW: 5 mg, 10 mg, and 20 mg. The removal rate was monitored over time, ranging from 0 to 60 min. The general trend observed is that as the mass of MDW increases, the removal rate of MB also increases. In all cases, a rapid initial adsorption phase was observed, with a significant portion of MB being removed within the first 10–20 min. This suggests that the active sites on the MDW are readily available for MB adsorption. After the initial rapid phase, the removal rate gradually slows down, eventually reaching a plateau. This indicates that the adsorption process has reached equilibrium, where the rate of MB adsorption is equal to the rate of desorption. The highest mass of MDW (20 mg) demonstrates the highest removal rate of 85.27% followed by 10 mg (70.89%) and 5 mg (57.48%) after 60 min of contact time. The equilibrium is reached at the highest percentage of MB removal among the three masses. The results suggest that MDW is a promising bioadsorbent for the removal of MB from aqueous solutions. Its ability to efficiently remove MB, especially at higher masses, highlights its potential for wastewater treatment applications.

The removal rate of various initial MB concentration using MDW is shown in Fig. 6(b). The removal rate is slower for higher initial MB concentrations (20 mg/L and 50 mg/L) compared to the lower concentration (10 mg/L). This is likely due to the fact that at higher concentrations, there are more MB molecules competing for adsorption sites on the MDW [81]. Despite the slower initial removal rates for higher concentrations, the final plateau levels are higher for higher initial MB concentration. Although the removal efficiency remained relatively stable across 20–50 mg/L initial MB concentrations, the adsorption capacity (Q_e) increased with concentration, indicating that MDW has sufficient active sites to accommodate higher dye loads. The consistent efficiency suggests good performance across a range of concentrations, rather than uniform adsorption quantities. In practical scenarios, dye concentrations in untreated textile and dyeing industry effluents can range from 10 to 200 mg/L, depending on the process and chemical loading involved [82]. The concentrations used in this study (20–100 mg/L) are therefore consistent with those commonly observed in real wastewater flows, particularly in high-strength dye effluents. By selecting this range, the adsorption performance of MDW was evaluated under conditions that closely mimic realistic industrial discharge scenarios.

pH is a critical parameter in adsorption processes, as it directly influences the surface charge of the adsorbent, the degree of ionization of functional groups, and the speciation of the adsorbate. Figure 6(c) illustrates the removal rate of MB from aqueous solutions at different pH values: 3, 6, and 10. The pH of the solution significantly affects the removal rate of MB. The highest removal rate was observed at pH 10, indicating that this pH is optimal for MB adsorption onto MDW. MB is a cationic dye, meaning it has a positive charge. In an alkaline environment, the surface of MDW becomes negatively charged due to deprotonation of

Table 1 Comparison of the PFO- and PSO adsorption rate constants, and calculated and experimental Q_e values

Adsorbent	Q_e, exp (mg/g)	PFO kinetic model			PSO kinetic model		
		K_1	$Q_{e,\ cal}$ (mg/g)	R^2	K_2	$Q_{e,\ cal}$ (mg/g)	R^2
DW	72.4	−0.00119	4.722555	0.9078	0.01216	73.53	0.999439
MDW	70	−0.00123	5.829901	0.99143	0.004986	73.09	0.99915

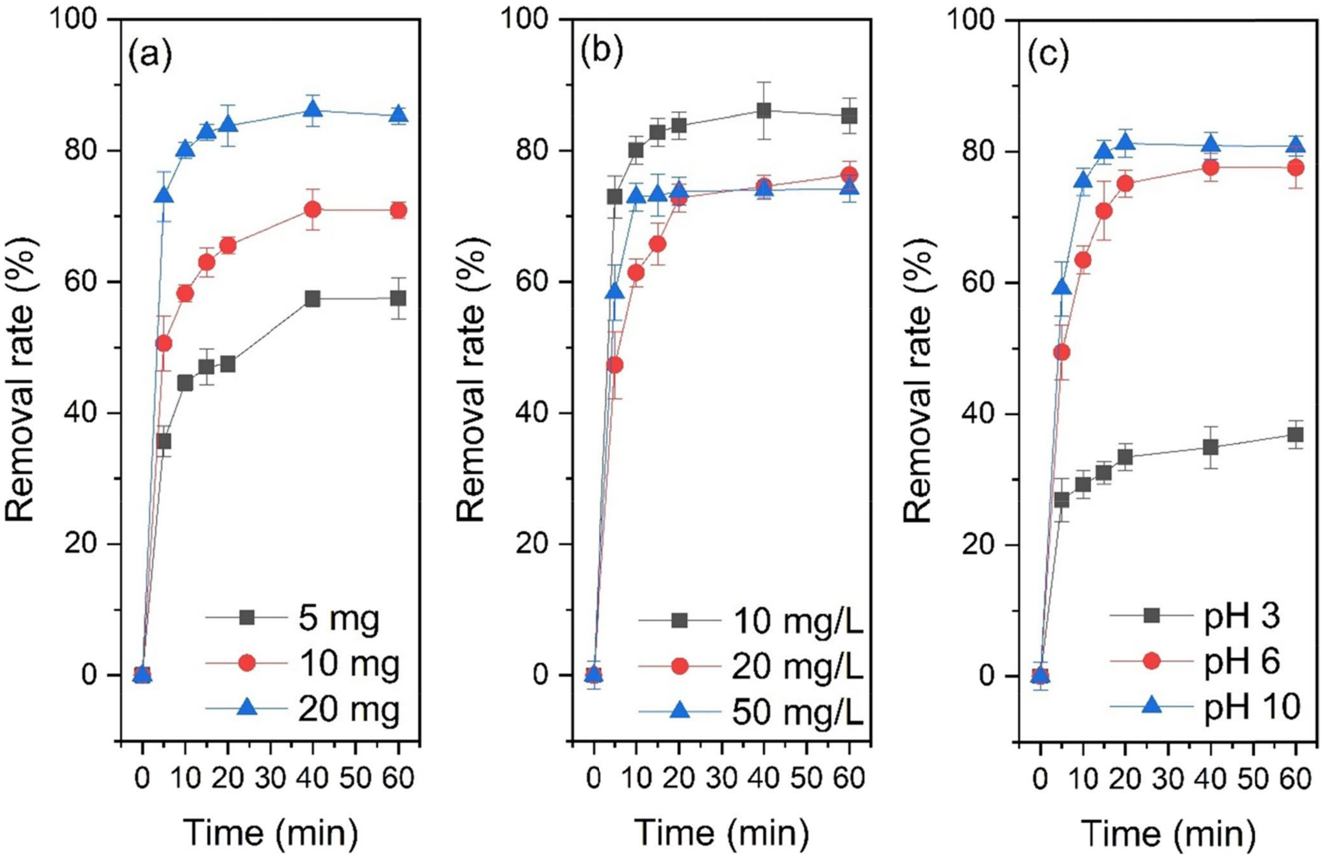

Fig. 6 MDW adsorption towards MB under various conditions (**a**) MDW dose (**b**) initial MB concentration. (**c**) solution pH

functional groups (e.g., hydroxyl, carboxyl groups) [45]. This negative surface charge enhances electrostatic attraction between the adsorbent and the positively charged MB, improving adsorption efficiency. At pH 3, the removal rate was relatively slow. This could be ascribed to the competition between hydrogen ions (H^+) and MB for adsorption sites on the MDW. The observed pH dependence suggests that the adsorption mechanism involves electrostatic interactions between the charged functional groups on the MDW and the MB molecules. The point of zero charge (pHz) of MDW was determined to be 6.8, indicating that the surface of MDW is positively charged at pH values below 6.8 and negatively charged at pH values above 6.8. This pHz value is critical in explaining the observed adsorption trends. At pH values below pHz, the surface of the MDW becomes positively charged, leading to electrostatic repulsion with the cationic MB molecules. In contrast, at pH values above pHz, the surface becomes negatively charged, favoring electrostatic attraction with MB [83]. This explains the observed increase in removal efficiency at alkaline pH levels, with optimal adsorption occurring around pH 10. The optimal adsorption observed at pH 10 as the increased deprotonation at higher pH levels maximizes the number of negatively charged active sites. The interaction is further supported by other mechanisms such as hydrogen bonding and π–π interactions, but the pH-dependent surface charge remains a dominant factor in the adsorption behavior.

3.1 Adsorption thermodynamics

The linear relationship observed in the van't Hoff plot shown in Fig. 7 confirms that the adsorption process is exothermic, as indicated by the negative values of ΔH° (−31.3946 kJ/mol). This result aligns with the characteristic behavior of exothermic adsorption processes, which may involve either physisorption or chemisorption. To distinguish between these two mechanisms, it is essential to analyze the absolute enthalpy values. Physisorption typically exhibits enthalpy values below 40 kJ/mol, whereas chemisorption is associated with higher enthalpy values, often exceeding 100 kJ/mol [84, 85]. The relatively low absolute value of ΔH° observed in this study strongly suggests that the adsorption of MB onto MDW is predominantly governed by physisorption.

The spontaneity of the adsorption process is further supported by the negative ΔG° values across all studied temperatures (298.15, 308.15, and 318.15 K). As shown in Table 2, ΔG° becomes less negative with increasing temperature,

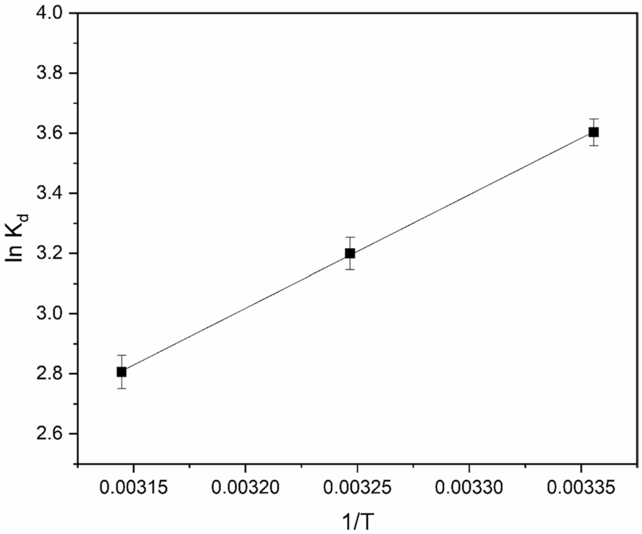

Fig. 7 Plot of ln K_d versus 1/T. Experimental conditions: Adsorbent dosage = 10 mg, Initial MB concentration = 10 mg/L, pH = 10, Contact time = 60 min

Table 2 Thermodynamic parameters obtained for MB adsorption on MDW

Temperature (K)	K_L	ΔG° (kJ/mol)	ΔH° (kJ/mol)	ΔS° (kJ/mol)	R^2
298.15	36.71027	−8.92683	−31.3946	−75.373	0.99971
308.15	24.52768	−8.19377			
318.15	16.54242	−7.41846			

indicating that lower temperatures favor the adsorption of MB onto MDW. This thermodynamic behavior suggests a stronger interaction between MB and MDW at lower temperatures. Additionally, the values of ΔG°, which are consistently less than −20 kJ/mol, point towards electrostatic interactions as the primary driving force for adsorption. Such interactions are characteristic of physisorption mechanisms and involve the attraction between charged MB molecules and the adsorbent surface.

The negative ΔS° (−75.373 J/mol·K) indicates a decrease in randomness at the solid-liquid interface during adsorption. This entropy reduction suggests an increased orderliness in the system, likely due to the alignment and immobilization of MB on the MDW surface. The formation of structured arrangements during adsorption is consistent with the cationic interactions between MB and the negatively charged sites on MDW. The high correlation coefficient (R^2 = 0.99971) obtained from the thermodynamic analysis validates the reliability of the data and the proposed adsorption mechanism. Overall, the thermodynamic parameters confirm that the adsorption of MB onto MDW is a spontaneous and exothermic process, as shown in Table 2.

3.2 Adsorption kinetics

The kinetics of this process were evaluated using three commonly employed models as shown in Fig. 8 (a-c): PFO, PSO, and Elovich, respectively. The PSO model exhibited the highest R^2, suggesting its superior fit to the experimental data. The poor fit of the PFO model highlights the insufficiency of simple diffusion-based adsorption to describe the observed behavior, emphasizing the complexity of the adsorption mechanism. The high R^2 value obtained for the PSO model as shown in Table 3 indicates that the adsorption of MB onto MDW is likely controlled by chemisorption rather than physical forces such as van der Waals interactions. This mechanism involves the formation of chemical bonds between the MB molecules and the functional groups on the MDW surface. Chemisorption involves valence forces, characterized by either electron sharing or exchange between the functional groups present on the biosorbent surface and the MB molecules [86, 87]. The strong interaction between the adsorbate and adsorbent is evident from the rapid initial adsorption rate observed in the experimental data. The MDW surface exhibits a high affinity for MB molecules, leading to a rapid and efficient adsorption process. The rate-limiting step in the adsorption process is likely the formation of chemical bonds between MB and MDW.

To further elucidate the adsorption mechanism, the Weber–Morris plot was applied by plotting Q_t versus $t^{1/2}$, as shown in Fig. 8(d).The plots reveal a multi-linear profile, which is commonly interpreted as a three-step adsorption process: (I) external surface diffusion or film diffusion, (II) gradual intraparticle diffusion into the porous structure of the adsorbent, and (III) equilibrium phase where diffusion slows and saturation is approached [88]. It can be seen that intraparticle diffusion is not the sole rate-limiting step, and that film diffusion and surface adsorption also contribute significantly to the overall kinetics. Furthermore, the extent of diffusion and adsorption capacity decreased with increasing temperature, suggesting that higher temperatures may hinder dye–adsorbent interaction, possibly due to reduced dye affinity or desorption effects. This analysis supports a complex, multi-mechanistic adsorption process involving both boundary layer and intraparticle mass transfer.

3.3 Adsorption isotherm

The isotherms were evaluated using three commonly employed models: Langmuir, Freundlich, and Temkin as shown in Fig. 9(a-c), respectively. The Temkin isotherm model exhibited the highest correlation coefficient (R^2), suggesting its superior fit to the experimental data. The high R^2 value obtained for the Temkin model shown in Table 4 indicates that the adsorption of MB onto MDW is likely

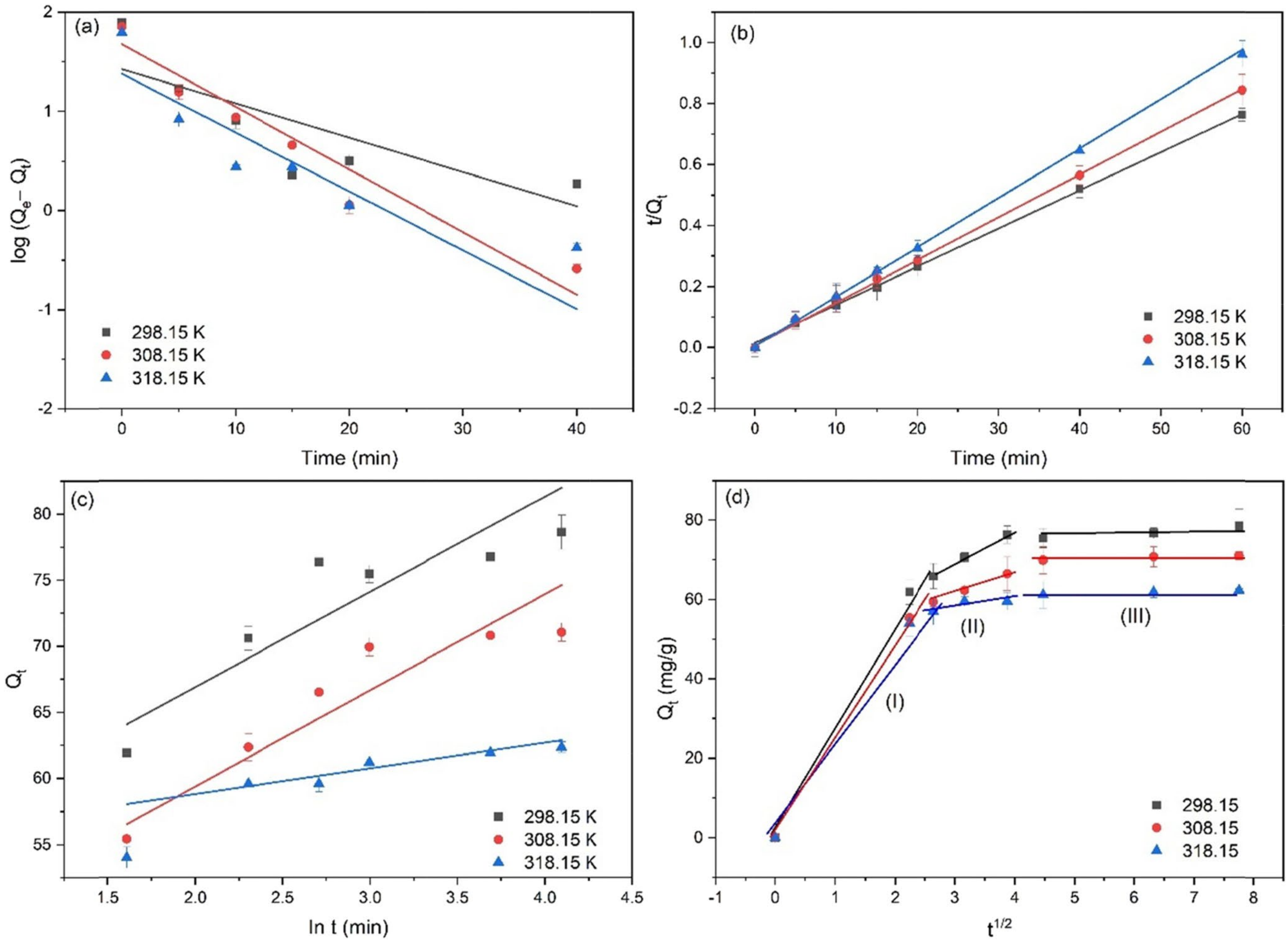

Fig. 8 (**a**) PFO (**b**) PSO (**c**) Elovich (**d**) Intra-particle diffusion (IPD) kinetic model. Experimental conditions: Adsorbent dosage = 10 mg, Initial MB concentration = 10 mg/L, pH = 10, Temperature = 25–45 °C

Table 3 Kinetic parameters for the sorption of MB onto MDW

Kinetic model	Parameters	MB adsorption		
		298.15	308.15	318.15
PFO	K_1	−0.0009	−0.00147	−0.00119
	$Q_{e, cal}$ (mg/g)	4.040991	4.794167	3.512366
	R^2	0.58244	0.91848	0.74945
PSO	K_2	0.014894	0.014262	0.031291
	$Q_{e, cal}$ (mg/g)	6268.928	5213.153	3935.712
	R^2	0.9993	0.99919	0.9998
Elovich	α	58333.4	13765.3	1852.98
	β	0.16469	0.1587	0.330507
	R^2	0.74274	0.82773	0.76607
IPD	K_1 (mg/g*min$^{-1/2}$)	25.83	23.23	22.42
	R^2	0.9919	0.9929	0.9905

characterized by a heterogeneous surface. This means that the adsorption sites on the MDW surface have varying energies, with some sites being more energetically favorable for adsorption than others. Temkin equilibrium binding constant (A) is related to the adsorption potential of the adsorbent. A higher value suggests stronger adsorbate-adsorbent interactions. Temkin constant (B) is related to the heat of adsorption, which indicates whether adsorption is endothermic or exothermic. Higher B value suggests that adsorption energy decreases more gradually, supporting adsorbate-adsorbent interactions rather than an abrupt saturation of active sites. The Temkin model effectively accounts for this heterogeneity, providing a more accurate description of the adsorption process [89]. Increased temperature can also lead to improved diffusion of adsorbate molecules within the adsorbent pores. This can facilitate mass transfer and improve adsorption efficiency.

3.4 Regeneration studies

The adsorbent exhibited excellent reusability, maintaining a high removal efficiency even after five consecutive adsorption-desorption cycles as shown in Fig. 10. The

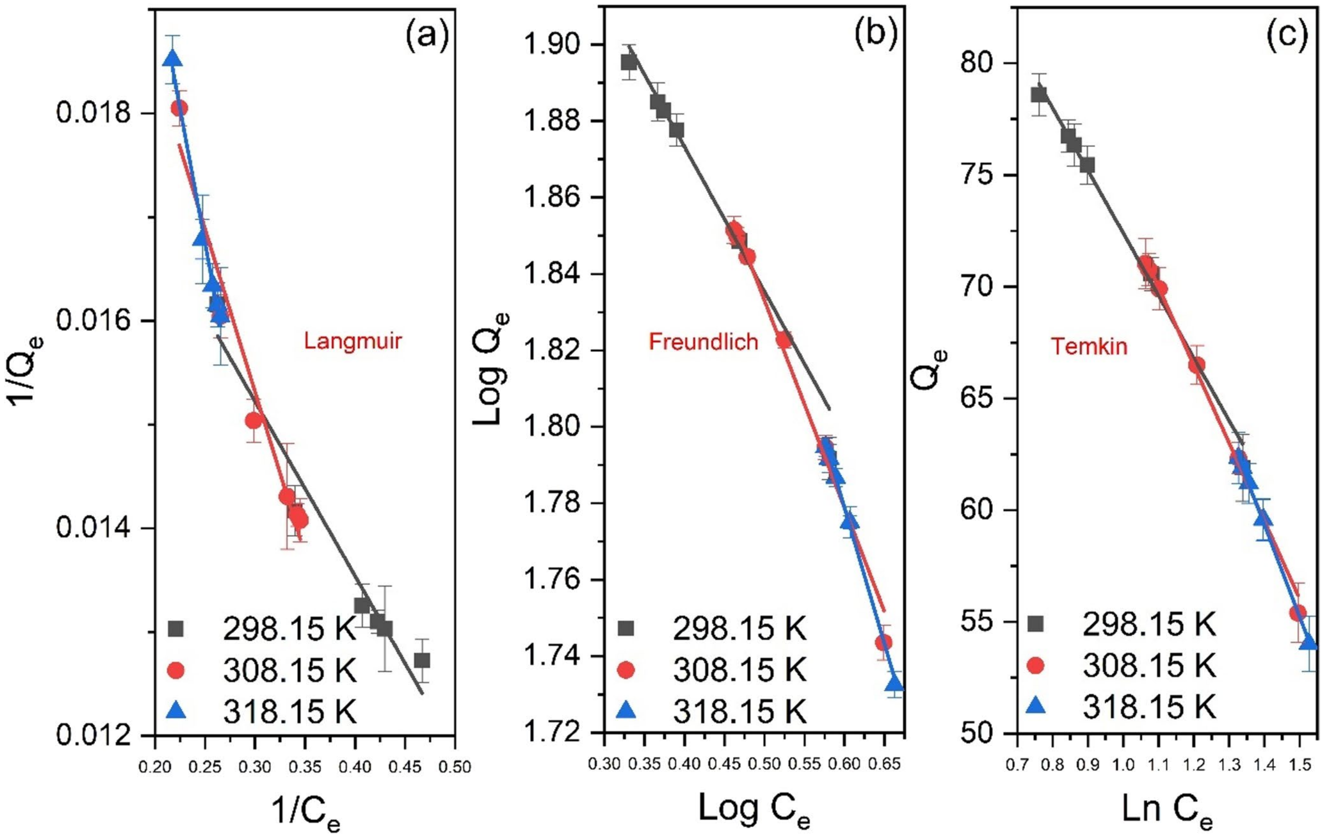

Fig. 9 Adsorption isotherm models. (**a**) Langmuir; (**b**) Freundlich and (**c**) Temkin. Experimental conditions: Adsorbent dosage = 10 mg, Initial MB concentration = 10 mg/L, pH = 10

Table 4 Parameters of isotherms for MB adsorption at different initial MB concentration

Model	Parameters	MB adsorption		
		298.15	308.15	318.15
Langmuir	Q_{max}	49.33399	40.43672	33.67003
	K_L	−1.2044	−0.78758	−0.57325
	R^2	0.94424	0.95731	0.98854
Freundlich	K_F	109.227	130.4848	162.6897
	n	−2.39406	−1.76688	−1.38635
	R^2	0.98612	0.9891	0.99714
Temkin	A	0.031	0.0471	0.0596
	B	−29.17329	−35.84902	−41.81207
	R^2	0.99285	0.99559	0.999

regeneration of the MDW adsorbent was performed using absolute ethanol (C_2H_5OH) as the desorbing agent, followed by rinsing with deionized water and drying before each reuse cycle. The adsorbent demonstrated moderate reusability, maintaining 69% of its initial adsorption capacity after five consecutive adsorption-desorption cycles, as shown in Fig. 10. Although there was a decrease in adsorption efficiency over cycles, MDW retained significant adsorption capability, indicating potential for practical wastewater treatment applications. The observed decline in removal efficiency after 5 cycles to approximately 69% is attributed to partial saturation of active sites due to incomplete desorption, minor structural degradation or pore blockage from repeated handling, and potential leaching of Fe_3O_4 NPs, which may reduce the material's adsorptive

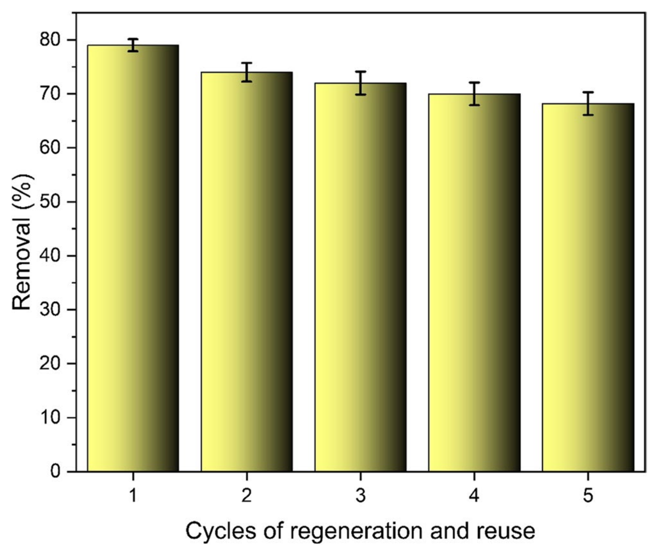

Fig. 10 Adsorption-desorption regeneration cycles for the repeated adsorption of MB onto MDW. Experimental conditions: Desorption agent = Ethanol, Contact time = 60 min, pH = 10

and magnetic properties over time [90]. The sustained performance of MDW over multiple cycles can be attributed to its unique properties. The magnetic nature of the adsorbent facilitates its easy separation from the treated wastewater, simplifying the recovery and reuse process. Additionally, the porous structure of MDW provides a large surface area, enhancing the adsorption capacity and promoting rapid diffusion of MB. The presence of functional groups on the MDW surface, such as hydroxyl and carboxyl groups, may also contribute to the adsorption process through electrostatic interactions and hydrogen bonding with the MB molecules. The observed slight decrease in removal efficiency after repeated cycles is likely due to the gradual accumulation of MB molecules on the adsorbent surface, which may hinder the accessibility of active adsorption sites. However, the overall performance of MDW remains impressive, suggesting its potential as a highly efficient and sustainable adsorbent for the removal of organic pollutants from wastewater.

3.5 Comparison of MB adsorption by various natural adsorbent

The MDW synthesized in this study represents a novel approach that combines the magnetic properties of Fe_3O_4 with the bio-derived porosity and functional groups of DW. DW offers unique advantages, such as rapid growth, abundant availability, and a naturally high content of oxygen-containing functional groups. The maximum adsorption capacity of MDW (78.59 mg/g) was in the upper middle level compared with the other biosorbents and were satisfactory for the removal of MB. When compared to the materials in the literature outlined in Table 5, such as Fe_3O_4/sugarcane bagasse (37.45 mg/g) [91] or Fe_3O_4/citrus bergamia BC (31 mg/g) [92], the MDW demonstrates a significant advantage in adsorption capacity. The adsorption capacities of the bioadsorbents vary significantly, with values ranging from as low as 0.02 mg/g for Fe_3O_4/Eucalyptus globulus BC [93] to an impressive 479.49 mg/g for

Table 5 MB adsorptive performance of MDW and various magnetic-based adsorbents

Adsorbent	Q_e (mg/g)	Adsorption kinetic	Adsorption isotherm	Adsorption thermodynamic	Recyclability/Regeneration	Ref
Fe_3O_4/alkali-modified tea	112.94	PSO	Langmuir	Non- spontaneous and exothermic	5 cycles/NR	[95]
Fe_3O_4/*Terminalia catappa* fruit kernel shell	90.89	PSO	Extended Langmuir	NR	5 cycles/90%	[86]
Fe_3O_4/sugarcane bagasse.	37.45	PSO	Langmuir	NR	NR	[91]
Fe_3O_4/peach gum bead	231.50	PSO	Langmuir	spontaneous and endothermic	6 cycles/>75%	[96]
$MnFe_2O_4$ encapsulated in *Scenedesmus obliquus*	12.50	PSO	Redlich-Peterson	spontaneous and exothermic	5 cycles/>90%	[97]
Fe_3O_4/*Eucalyptus globulus* BC	0.02	PSO	Langmuir	non-spontaneous and endothermic	NR	[93]
Fe_3O_4/green tea residue BC	394.30	PSO	Dubinin-Radushkevich	spontaneous and endothermic	5 cycles/66%	[98]
Ni/wakame BC	479.49	PSO	Langmuir	spontaneous and endothermic	5 cycles/74.2%	[94]
Fe_3O_4/citrus bergamia BC	31	PSO	Langmuir	spontaneous and endothermic	5 cycles/69.8%	[92]
Fe_3O_4/hawthorn seeds BC	147.00	PSO	Langmuir	spontaneous and endothermic	NR	[99]
Fe_3O_4/oxidized candle soot	237.18	PSO	NR	NR	5 cycles/90%	[100]
Fe_3O_4/reed BC	354.40	NR	Langmuir	spontaneous and endothermic	5 cycles/74%	[101]
Fe_2O_3/*Lagenaria siceraria* BC	54.44	PSO	Langmuir	spontaneous and endothermic	4 cycles/27%	[102]
Fe_3O_4/waste areca nut husk BC	785.34	PSO	Langmuir	NR	4 cycles/40.25%	[103]
Fe_3O_4/*Tagetes erecta* BC	113.35	PSO	Langmuir	spontaneous and endothermic	5 cycles/52%	[104]
MDW	78.59	PSO	Temkin	spontaneous and exothermic	5 cycles/69%	**This study**

NR not reported, *BC* biochar

Ni/wakame BC [94]. These differences can be attributed to the structural and chemical characteristics of the bioadsorbents, as well as the presence of functional groups that facilitate interaction with MB molecules. The superior fit of the Temkin model for MDW contrasts with the Langmuir dominance observed in most other studies, suggesting that MDW's adsorption mechanism benefits from its unique surface heterogeneity and functionalization. In addition, it also suggests that adsorption is influenced by both electrostatic forces and adsorbate-adsorbent interactions.

3.6 Proposed MB adsorption mechanism

The adsorption of MB onto MDW involves a multi-faceted mechanism driven by the physicochemical interactions between MB molecules and the MDW surface. The adsorption process follows a two-phase behavior: an initial rapid uptake, attributed to the abundance of available active sites, followed by a slower phase as equilibrium is approached, likely due to saturation of these sites [105]. Briefly, the adsorption mechanism involves several steps: (i) The MB molecules move from the solution to the surface of MDW. (ii) MB diffuses through the boundary layer to reach the adsorbent surface. (iii) MB are then captured by active adsorption sites on the MDW.

At pH values above the point of zero charge (pHz = 6.8), the surface of MDW becomes negatively charged due to deprotonation of functional groups such as hydroxyl and carboxyl groups. This negative surface charge strongly attracts the cationic MB^+ molecules through electrostatic interactions [106–108]. The pH-dependent adsorption efficiency observed in this study highlights the critical role of electrostatic forces, with optimal adsorption occurring in alkaline conditions (pH 10), where the deprotonation of surface groups is maximized. At pH < 6.8, MDW carries a partial positive charge, reducing adsorption due to electrostatic repulsion between MB and the adsorbent. As contact time increases, the resistance of the boundary layer decreases, which boosts the mobility of MB molecules during adsorption. Since MB uptake at the active sites of MDW occurs rapidly, the process is largely controlled by the rate of mass transfer in the liquid phase. SEM image depicted in Fig. 2(b) revealed that MDW has a rough, porous structure, which also may promote efficient physical adsorption. The presence of micro- and mesopores enhances the physical entrapment of dye molecules, complementing electrostatic forces.

MB contains three aromatic rings with delocalized π-electrons and a positively charged center, while MDW has π-electron-rich carbon structures and defects. The mechanisms contributing to the adsorption of MB onto MDW may include electrostatic interactions: At higher pH values, specifically at pH 10, MB^+ is the dominant species, which is strongly attracted to the negatively charged MDW surface; evident from the highest adsorption capacity. The presence of functional groups, such as phenolic and carbonyl groups (as confirmed by FTIR analysis), enhances these π–π stacking interactions, contributing to the overall adsorption capacity. MB contains aromatic rings, and MDW has π-electron-rich carbon structures, leading to π–π stacking interactions that further stabilize dye adsorption. This interaction is particularly significant for maintaining high adsorption efficiency even at elevated MB concentrations [109, 110].

Hydrogen bonding plays a supplementary role in the adsorption process, as evidenced by the shifts and broadening of the O–H stretching peaks in the FTIR spectra of MDW after adsorption. These interactions occur between the hydrogen atoms in the MDW functional groups and the nitrogen atoms in the MB molecules, further stabilizing the adsorbate-adsorbent complex. The SEM analysis also revealed that MDW possesses a porous structure with visible voids and defects. These features enhance the physical adsorption of MB molecules by providing additional active sites and increasing the surface area available for interaction. Additionally, the defects may serve as trapping sites for MB molecules, contributing to the rapid initial uptake observed in kinetic studies.

The most prevalent interaction is dipole-dipole hydrogen bonding between the oxygen (O) and nitrogen (N) atoms on the MDW and the nitrogen atoms in the MB. The second type involves Yoshida hydrogen bonding, occurring between the aromatic rings of the dyes and the O─H and N─H groups present on the MDW. Additionally, (n-π) interactions may also occur, wherein the lone pair electrons on an oxygen atom are delocalized into the π-orbital of the aromatic dye ring [97]. Thus, the adsorption of MB onto MDW is driven by a combination of electrostatic forces, π–π interactions, hydrogen bonding, and the trapping of dye molecules by structural defects which is summarized in Fig. 11. The adsorption mechanism is further supported by thermodynamic studies, which indicate that the process is exothermic and spontaneous.

The removal of MB by MDW proceeds through coupled interfacial processes governed by surface charge behavior, surface functional groups, and aromatic interactions, as summarized below.

Step 1. Surface ionization under alkaline condition.

$$MDW–OH \rightleftharpoons DW–O^- + H^+$$

$$MDW–COOH \rightleftharpoons DW–COO^- + H^+$$

Step 2. Electrostatic attraction and surface anchoring.

$$MDW–O^- + MB^+ \rightarrow DW–O^- \cdots MB^+$$

$$MDW–COO^- + MB^+ \rightarrow DW–COO^- \cdots MB^+$$

Step 3. Surface coordination on magnetite sites.

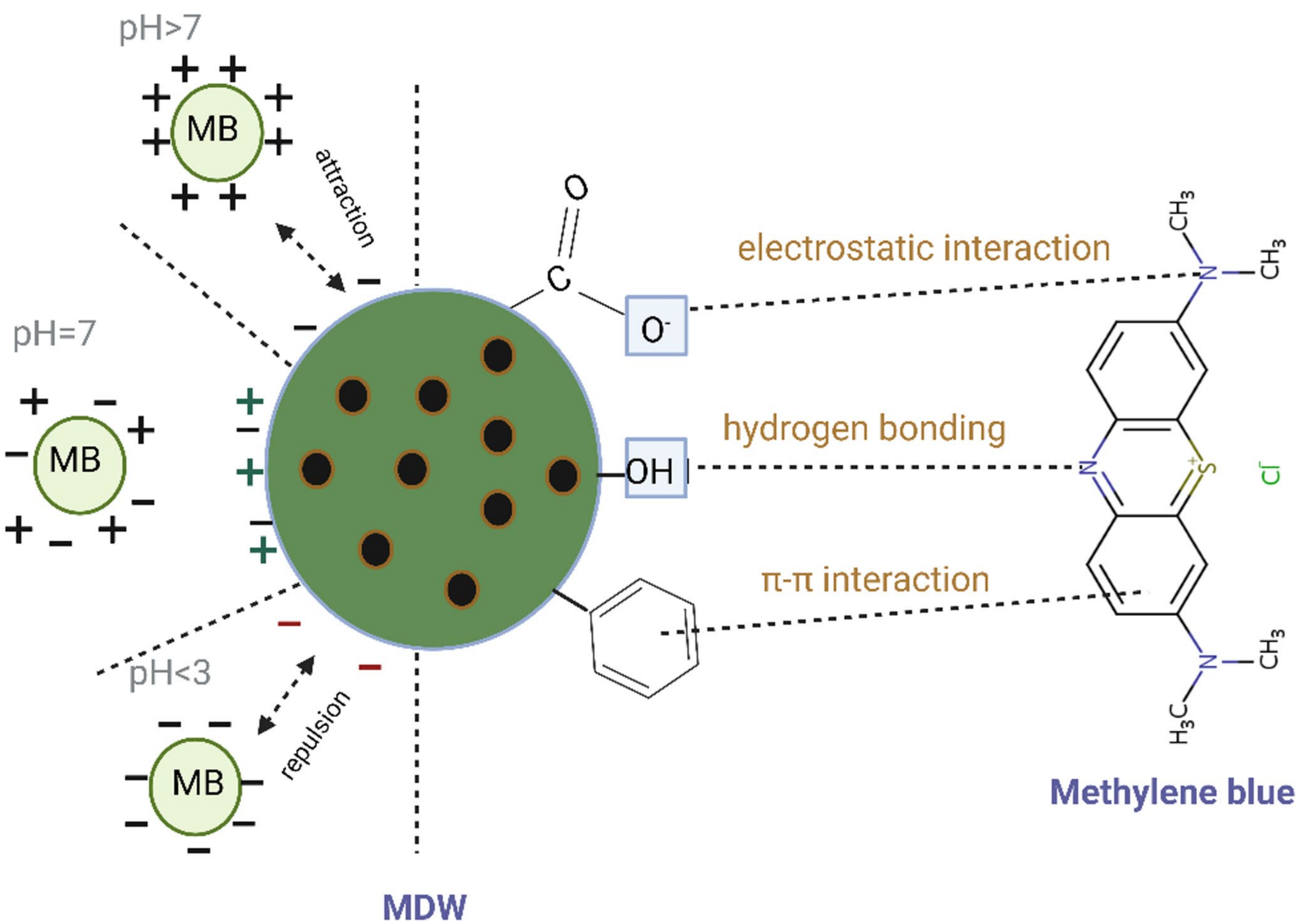

Fig. 11 Proposed adsorption mechanism of MB on MDW

≡Fe–OH + MB^+ ⇌ ≡Fe–O···MB + H^+
Step 4. π–π interaction between aromatic systems.
C(aromatic)|| MB(aromatic) → π–π complex
C(aromatic)|| MB(aromatic) → π–π complex
Step 5. Hydrogen bonding.
MDW–OH···N(MB)
MDW–COOH···N(MB)
Step 6. Intraparticle diffusion and pore capture.
MB (solution) → MB (surface) → MB (pore)

3.7 Anti-bacterial study

Previous studies have shown that magnetite NPs exhibit significant antibacterial properties, making them promising alternatives to traditional antibiotics. Magnetite showed enhanced antibacterial activity against resistant strains of bacteria, such as *Staphylococcus aureus* and *Escherichia coli* [111]. Based on Fig. 12, no to little inhibition zone was observed around the MDW sample, indicating a lack of antibacterial activity against Gram positive (*E. coli* and *P. putida*) and Gram negative (*S. aureus* and *B. cereus*) bacteria strain. The green synthesis process using AA might have inadvertently inactivated or degraded any bioactive compounds present in the MDW that could have antibacterial properties. The green synthesis of MDW involves the use of AA that can act as capping agents. These agents can influence the surface properties and stability of NPs, potentially hindering their interaction with bacterial cells. For instance, proteins and other biomolecules used in the synthesis can form a coating that reduces the NPs' ability to penetrate bacterial cell walls [112]. Bacteria like *E. coli* and *S. aureus* can form biofilms, which are protective layers that shield them from external threats, including NPs. This biofilm can prevent NPs from reaching the bacterial cells, thus nullifying their antibacterial effects [113]. The MDW may have reduced toxicity and this attribute offers a distinct advantage from an environmental and human health perspective. Alternatively, the concentration of MDW used in the assay may have been insufficient to exert an inhibitory effect. As shown in Table 6, the zone of inhibition around the MDW disks was comparable to that of the negative control, ethanol.

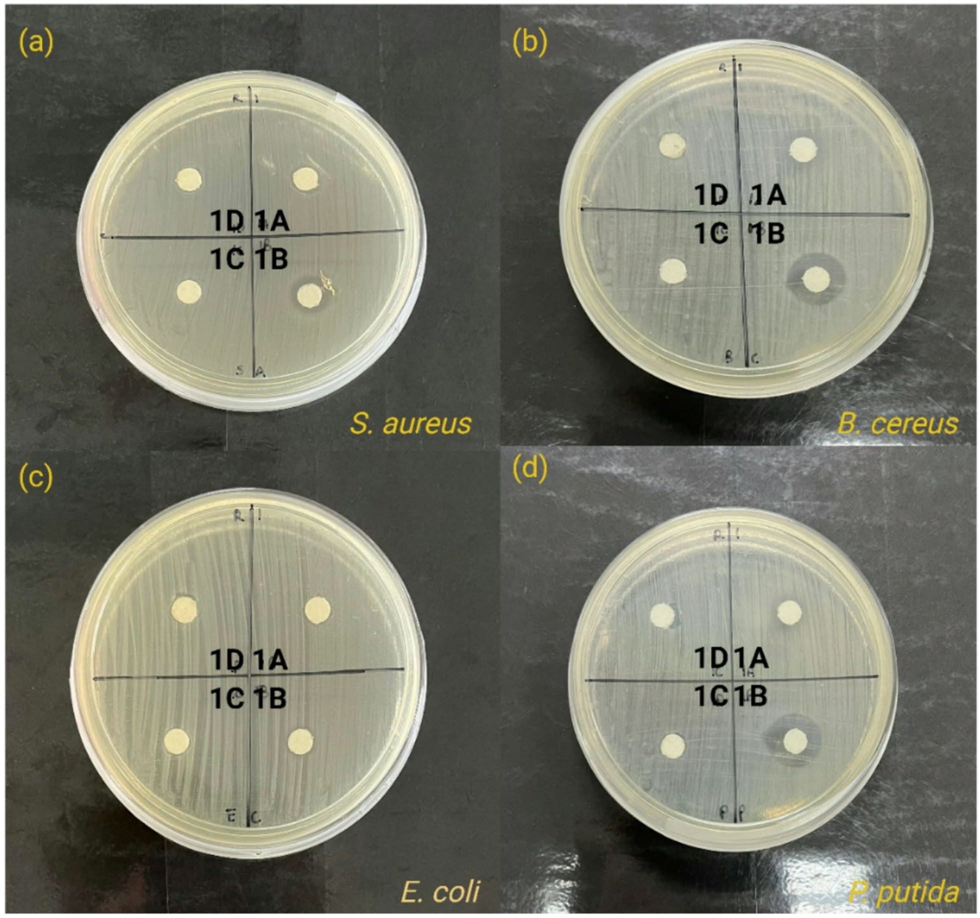

Fig. 12 Inhibition zone test results for MDW on (**a**) *S. aureus*; (**b**)*B. cereus;* (**c**) *E. coli*; (**d**) *P. putida*. Zone 1**A**: water (-ve control), 1**B**: streptomycin (+ve control), 1**C**: ethanol (-ve control), 1**D**: sample

Table 6 Antibacterial activity of the MDW (zone of Inhibition in millimeter)

Sample	Staphylococcus aureus	Bacillus cereus	Escherichia coli	Pseudomonas putida
Water	NA	NA	NA	NA
Streptomycin	8.92±0.82	14.00±0.41	7.33±0.31	14.08±0.31
Ethanol	6.92±0.12	6.83±0.47	6.92±0.32	7.08±0.31
MDW	7.00±0.01	6.83±0.24	7.17±0.31	7.33±0.12

Values are expressed as mean±SD of three replicates

NA Not active

3.8 Cost estimation

The cost estimation for the production of MDW was conducted to evaluate its economic feasibility for large-scale applications [114–116]. The synthesis process utilized locally sourced DW which was collected at no cost, and low-cost chemicals, making the approach both affordable and sustainable. Table 7 outlines the breakdown of costs for the key components and steps involved in the synthesis of MDW. The DW was freely collected from a retention pond, eliminating costs associated with raw material acquisition. In this study, the collection of DW was conducted at a laboratory scale, where no direct costs were incurred as students performed the collection process. Therefore, the cost of raw material collection was assumed to be zero in this analysis. However, for large-scale industrial applications, the collection, transportation, and handling of biomass would involve costs, which should be considered when evaluating the economic feasibility of commercial production. This highlights the economic advantage of using abundant and renewable biomass sources. The primary chemicals involved in the synthesis process include ferrous sulfate, KOH, and AA. The use of AA, a cost-effective and environmentally friendly reducing agent, significantly reduced the dependency on more expensive and hazardous chemicals like hydrazine. Unlike many previously reported methods that require elevated temperatures or the use of harsh chemicals, the co-precipitation method eliminates the need for high-temperature heating, significantly reducing the energy input required for synthesis. The energy costs for drying, magnetic stirring, and oven-drying were estimated based on the power ratings of the equipment and the duration of operation. These processes collectively accounted for RM 28.56 per kg or 96.78% from the total cost of goods sold, making up a significant portion of the overall cost. On a laboratory scale, labor and transportation costs were negligible, but these may scale differently in industrial production. The

Table 7 Estimated cost analysis of 1 kg MDW synthesis

Materials/Chemicals	Process	Unit	Price per unit (RM per unit)	Total cost (RM)
MDW	Collection using net and plastic pail	5 kg (wet)	Duckweed (DW) were collected free of cost from retention pond in Bintulu	0.00
	Washing of raw material	0.05 m^3	2.62 per m^3 #	0.13
	Sun drying of DW	108 h	0.00	0.00
	Oven drying of DW	1.5 kWh X 24 h = 36 kWh	0.39 per kWh***	14.04
	Magnetic stirring process in MDW synthesis	0.2 kWh X 2 h = 0.4 kWh	0.39 per kWh***	0.12
	Oven drying of MDW	1.5 kWh X 24 h = 36 kWh	0.39 per kWh***	14.04
	Grinding into fine powder	0.29 kWh X 2 h = 0.58 kWh	0.39 per kWh***	0.23
	Total Cost of MDW processing			**RM 28.56**
Chemicals	$FeSO_4 \cdot 7H_2O$	3.475 g	54.00/500 g	RM 0.38
	AA	1.32 g	28.00/100 g	RM 0.37
	KOH	2.81 g	70.00/kg	RM 0.20
	Total Chemical Cost			**RM 0.95**
Total Cost of Goods Sold				**RM 29.51**

*** refer to Tenaga Nasional Berhad tariff rate. # referred to Air Selangor tariff rate

cost analysis only covered the cost of goods sold and did not include other operational costs such as labour and transportation cost, as the focus was primarily on materials and energy. The estimated total cost of producing 5 kg wet DW to 1 kg MDW was approximately RM 29.51 per kg. This is highly competitive when compared to other magnetic adsorbents converted to BC, which often require more expensive precursors/activation agents or energy-intensive synthesis methods, such as pyrolysis.

3.9 Strengths, limitations, and recommendations for future research

This study offers several notable strengths, particularly the development of a sustainable, low-cost MDW-based adsorbent synthesized via a green co-precipitation method using AA, which enhances its environmental friendliness. The research presents a comprehensive performance evaluation of MDW, encompassing kinetic, isotherm, and thermodynamic behavior, as well as regeneration potential and cost analysis, all supported by key characterization techniques including SEM, FTIR, and XRD. However, some limitations should be acknowledged. The study did not include advanced characterization methods such as BET, TEM, or XPS, which could have provided deeper insights into surface area, nanostructure, and surface chemistry due to equipment constraints. Additionally, adsorption experiments were limited to MB as a model dye, and regeneration was evaluated over only five cycles. Real industrial wastewater was not used, limiting immediate field applicability.

To address these gaps, future research should incorporate advanced material characterization techniques to better understand surface properties and adsorption mechanisms. Broader testing with other dye types—including anionic, neutral, and mixed dyes will be necessary to evaluate the versatility and selectivity of MDW. Regeneration studies should be extended to more than five cycles to assess long-term adsorbent durability and structural integrity. Furthermore, the temperature range used for adsorption testing (298–318 K) reflects typical industrial discharge conditions in warm climates; however, performance under cooler temperatures (e.g., 288–293 K or 15–20 °C) remains unexplored. Such testing is essential for assessing MDW's applicability in temperate or seasonal environments, where diffusion rates and adsorption kinetics may differ. Similarly, the thermodynamic analysis was limited to three temperature points, which restricts the precision of Van't Hoff-derived parameters; future studies should include additional temperature intervals to improve the reliability of ΔH° and ΔS° estimates.

Future work should also extend the pH range, including alkaline conditions beyond pH 8, to define adsorption behavior near and above the point of zero charge and identify performance boundaries under realistic industrial conditions. Assessment of environmental safety should also examine Fe_3O_4 leaching under varying pH and ionic strength using ICP-MS, alongside evaluation of interaction with natural organic matter to establish long-term operational stability. Within this context, the present study demonstrates clear commercial relevance through feedstock selection, synthesis design, cost control, and operational performance. Duckweed serves as a low-cost biomass resource with consistent availability and transforms routine waterway maintenance waste into treatment material. The synthesis approach avoids thermal carbonisation and hazardous reagents, while low-temperature co-precipitation with ascorbic acid reduces energy demand and chemical risk. The estimated cost of RM 29.51 per kg supports industrial adoption. Magnetic recovery eliminates filtration and centrifugation, improving throughput and reducing maintenance, and regeneration retains more than 69% performance after five cycles. The structure and surface chemistry of MDW also support binding of cationic metals and pharmaceuticals, extending use toward mixed industrial effluents. Collectively, these attributes position MDW as a practical adsorbent system suitable for scale-up across centralized and decentralized wastewater treatment settings.

4 Conclusion

This study demonstrates the successful development of a MDW-based adsorbent through green co-precipitation using AA as the reducing agent. The material achieved a maximum MB adsorption capacity of 78.59 mg/g and showed the practical advantage of magnetic recovery. Adsorption followed the PSO model and was best described by the Temkin isotherm, confirming heterogeneous surface interactions governed by electrostatic attraction, hydrogen bonding, and π–π interactions. Thermodynamic evaluation confirmed spontaneous and exothermic adsorption, with highest efficiency under alkaline conditions. Magnetic separation enabled direct recovery without filtration, improving operational simplicity. Regeneration preserved more than 69% removal efficiency after five cycles, while cost analysis estimated production at RM 29.51/kg, supporting economic feasibility. The combination of green synthesis, magnetic separability, stable performance, and low production cost positions MDW as a deployable adsorbent system for dye-contaminated wastewater. This work establishes a scalable pathway for converting nuisance biomass into functional remediation material.

Supplementary information The online version contains supplementary material available at https://doi.org/10.1007/s13399-025-06946-2.

Acknowledgements We would like to thank the Department of Sewerage Services, Sarawak for allowing access (SSD/OPM/BTU/2-Vol.2(17)) to the retention pond and collect the duckweed samples.

Author contributions KWKS contributed to the study conception and analysis. ALTZ contributed to the study conception and wrote the first draft of the manuscript. KBJ contributed in the analysis. TTH and ELTC provided resource and reviewed the manuscript. JL carried out analysis and investigation. YA provided resource, supervision, and reviewed the manuscript All authors read and approved the final manuscript.

Funding Open access funding provided by The Ministry of Higher Education Malaysia and Universiti Putra Malaysia. This work was supported by Sarawak Research and Development Council under the Research Initiation Fund (RDCRG01/RIF/2023/_156). The authors confirm that there are no additional funders. The funder had no role in study design, data collection and analysis, decision to publish, or preparation of the manuscript.

Data availability Data will be made available on request.

Declarations

Ethics approval Not applicable.

Consent to participate This investigation has the approval from the Sarawak Biodiversity Centre (SBC).

Consent for publication All authors reviewed and agreed to the final manuscript for publication.

Competing interest The authors declare that they have no known competing financial interests or personal relationships that could have appeared to influence the work reported in this paper.

References

1. Zahakifar F, Keshtkar AR, Talebi M (2021) Performance evaluation of sodium alginate/polyvinyl alcohol/polyethylene oxide/ZSM5 zeolite hybrid adsorbent for ion uptake from aqueous solutions: a case study of thorium (IV). J Radioanal Nucl Chem 327:65–72. https://doi.org/10.1007/s10967-020-07479-w
2. Zahakifar F, Keshtkar AR, Talebi M (2021) Synthesis of sodium alginate (SA)/ polyvinyl alcohol (PVA)/ polyethylene oxide (PEO)/ ZSM-5 zeolite hybrid nanostructure adsorbent by casting method for uranium (VI) adsorption from aqueous solutions. Prog Nucl Energy 134:103642. https://doi.org/10.1016/j.pnucene.2021.103642
3. Khan NA, Saeed K, Khan I et al (2022) Efficient photodegradation of orange II dye by nickel oxide nanoparticles and nanoclay supported nickel oxide nanocomposite. Appl Water Sci 12:131. https://doi.org/10.1007/s13201-022-01647-x
4. Khan AU, Zahoor M, Rehman MU et al (2022) Biological mineralization of Methyl Orange by *Pseudomonas aeruginosa*. Water 14:1551. https://doi.org/10.3390/w14101551

5. Oyetade JA, Van Hulle SWH, Hammond VNK et al (2024) Process modeling and optimization of photocatalytic treatment of dye-polluted effluent using novel polyaniline/graphene oxide-Fe3O4-Ag nanocomposites. J Water Process Eng 68:106548. https://doi.org/10.1016/j.jwpe.2024.106548
6. Oyetade JA, Machunda RL, Hilonga A (2022) Photocatalytic degradation of azo dyes in textile wastewater by Polyaniline composite catalyst-a review. Sci Afr 17:e01305. https://doi.org/10.1016/j.sciaf.2022.e01305
7. Oyetade JA, Machunda RL, Hilonga A (2024) Fenton-mediated solar-driven photocatalysis of industrial dye effluent with polyaniline impregnated with activated TiO2-Nps. J Photochem Photobiol 20:100231. https://doi.org/10.1016/j.jpap.2024.100231
8. Dabagh A, Ait Ichou A, Benhiti R et al (2024) Removal of methylene blue from aqueous solutions by adsorption onto *Carpobrotus edulis* biomass. Bioremediat J 1–16. https://doi.org/10.1080/10889868.2024.2382266
9. Dabagh A, Abali M, Ait Ichou A et al (2023) Optimization and modeling of adsorption of Congo Red and Rhodamine B dyes onto *Carpobrotus edulis* plant. J Dispers Sci Technol 44:2429–2438. https://doi.org/10.1080/01932691.2022.2093215
10. Luo X-P, Fu S-Y, Du Y-M et al (2017) Adsorption of methylene blue and malachite green from aqueous solution by sulfonic acid group modified MIL-101. Microporous Mesoporous Mater 237:268–274. https://doi.org/10.1016/j.micromeso.2016.09.032
11. Elshimy AS, Mobarak M, Ajarem JS et al (2024) Sodium alginate-modified alkali-activated eggshell/Fe3O4 nanoparticles: a magnetic bio-based spherical adsorbent for cationic dyes adsorption. Int J Biol Macromol 256:128528. https://doi.org/10.1016/j.ijbiomac.2023.128528
12. Oladoye PO, Ajiboye TO, Omotola EO, Oyewola OJ (2022) Methylene blue dye: toxicity and potential elimination technology from wastewater. Results Eng 16:100678. https://doi.org/10.1016/j.rineng.2022.100678
13. Balarak D, Ganji F, Choi SS et al (2019) Effects of operational parameters on the removal of acid blue 25 dye from aqueous solutions by electrocoagulation. Appl Chem Eng 30:742–748. https://doi.org/10.14478/ace.2019.1092
14. Balarak D, Abasizadeh H, Yang J-K et al (2020) Biosorption of Acid Orange 7 (AO7) dye by canola waste: equilibrium, kinetic and thermodynamics studies. Desalin Water Treat 190:331–339. https://doi.org/10.5004/dwt.2020.25665
15. Balarak D, Zafariyan M, Igwegbe CA et al (2021) Adsorption of Acid Blue 92 Dye from Aqueous Solutions by Single-Walled Carbon Nanotubes: Isothermal, Kinetic, and Thermodynamic Studies. Environ Process 8:869–888. https://doi.org/10.1007/s40710-021-00505-3
16. Al-Musawi TJ, Rajiv P, Mengelizadeh N et al (2021) Development of sonophotocatalytic process for degradation of acid orange 7 dye by using titanium dioxide nanoparticles/graphene oxide nanocomposite as a catalyst. J Environ Manage 292:112777. https://doi.org/10.1016/j.jenvman.2021.112777
17. Balarak D, Al-Musawi TJ, Mohammed IA, Abasizadeh H (2020) The eradication of reactive black 5 dye liquid wastes using *Azolla filiculoides* aquatic fern as a good and an economical biosorption agent. SN Appl Sci 2:1015. https://doi.org/10.1007/s42452-020-2841-x
18. Zheng ALT, Andou Y (2022) Hybrid three-dimensional (3D) graphene architectures for photocatalysis of noxious pollutants. In: Pal K (ed) Green nanoarchitectonics. Jenny Stanford Publishing, New York, pp 47–72
19. Zheng ALT, Boonyuen S, Andou Y (2023) Porous graphene-based materials for enhanced adsorption towards emerging micropollutants (EMs). In: Handbook of Porous Carbon Materials. pp 547–570
20. Zheng ALT, Ohno T, Andou Y (2022) Recent progress in photocatalytic efficiency of hybrid three-dimensional (3D) graphene architectures for pollution remediation. Top Catal 65:1634–1647. https://doi.org/10.1007/s11244-022-01610-9
21. Zheng ALT, Teo EYL, Seenivasagam S et al (2024) Nanostructures embedded on porous materials for the catalytic reduction of nitrophenols: a concise review. J Porous Mater 31:1557–1575. https://doi.org/10.1007/s10934-024-01618-4
22. Zheng ALT, Sabidi S, Ohno T et al (2022) Cu2O/TiO2 decorated on cellulose nanofiber/reduced graphene hydrogel for enhanced photocatalytic activity and its antibacterial applications. Chemosphere 286:131731. https://doi.org/10.1016/j.chemosphere.2021.131731
23. Shanmugam P, Parasuraman B, Boonyuen S et al (2024) Hydrothermal synthesis and photocatalytic application of ZnS-Ag composites based on biomass-derived carbon aerogel for the visible light degradation of methylene blue. Environ Geochem Health 46:92. https://doi.org/10.1007/s10653-024-01871-1
24. Lau GE, Che Abdullah CA, Wan Ahmad WAN et al (2020) Eco-friendly photocatalysts for degradation of dyes. Catalysts 10:1129. https://doi.org/10.3390/catal10101129
25. Periyasamy AP (2024) Recent advances in the remediation of textile-dye-containing wastewater: prioritizing human health and sustainable wastewater treatment. Sustainability 16:495. https://doi.org/10.3390/su16020495
26. Satyam S, Patra S (2024) Innovations and challenges in adsorption-based wastewater remediation: a comprehensive review. Heliyon 10:e29573. https://doi.org/10.1016/j.heliyon.2024.e29573
27. Zheng ALT, Boonyuen S, Ohno T, Andou Y (2021) Hydrothermally reduced graphene hydrogel intercalated with divalent ions for dye adsorption studies. Processes 9:169. https://doi.org/10.3390/pr9010169
28. Zheng ALT, Che Abdullah CA, Andou Y (2023) Graphene-based nanomaterials for water remediation applications. In: Shanker U, Hussain CM, Rani M (eds) Handbook of green and sustainable nanotechnology. Springer International Publishing, Cham, pp 1097–1122
29. Zheng ALT, Teo EYL, Seenivasagam S et al (2024) Recent review on porous adsorbents for water decontamination: strategies for enhanced removal of tetracycline. J Porous Mater. https://doi.org/10.1007/s10934-024-01699-1
30. Zheng ALT, Sinin AE, Jin WT et al (2024) Rare earth elements for enhancing photocatalysis in pollutant degradation and water treatment. Int J Environ Sci Technol. https://doi.org/10.1007/s13762-024-06203-5
31. Zheng ALT, Teo EYL, Marzuki OF et al (2025) Additive manufacturing of high-performance adsorbents for environmental use. Eng Res Express 7:032001. https://doi.org/10.1088/2631-8695/adfacc
32. Reza MS, Yun CS, Afroze S et al (2020) Preparation of activated carbon from biomass and its' applications in water and gas purification, a review. Arab J Basic Appl Sci 27:208–238. https://doi.org/10.1080/25765299.2020.1766799
33. Egun IL, He H, Hu D, Chen GZ (2022) Molten salt carbonization and activation of biomass to functional biocarbon. Adv Sustain Syst. https://doi.org/10.1002/adsu.202200294
34. Malini K, Selvakumar D, Kumar NS (2023) Activated carbon from biomass: preparation, factors improving basicity and surface properties for enhanced CO2 capture capacity – a review. J CO2 Util 67:102318. https://doi.org/10.1016/j.jcou.2022.102318
35. Vafakish B, Babaei-Ghazvini A, Acharya B (2024) Unraveling the mechanisms of methylene blue adsorption onto biochar: a robust and sustainable approach for water remediation. Int J Environ Sci Technol. https://doi.org/10.1007/s13762-024-06111-8

36. Ge Q, Li P, Liu M et al (2023) Removal of methylene blue by porous biochar obtained by KOH activation from bamboo biochar. Bioresour Bioprocess 10:51. https://doi.org/10.1186/s40643-023-00671-2
37. Akhtar MS, Ali S, Zaman W (2024) Innovative adsorbents for pollutant removal: exploring the latest research and applications. Molecules 29:4317. https://doi.org/10.3390/molecules29184317
38. Al-Najar JA, Al-Humairi ST, Lutfee T et al (2023) Cost-Effective Natural Adsorbents for Remediation of Oil-Contaminated Water. Water 15:1186. https://doi.org/10.3390/w15061186
39. GadelHak Y, El-Azazy M, Shibl MF, Mahmoud RK (2023) Cost estimation of synthesis and utilization of nano-adsorbents on the laboratory and industrial scales: a detailed review. Sci Total Environ 875:162629. https://doi.org/10.1016/j.scitotenv.2023.162629
40. Zheng ALT, Rajoo KS, Manivel CM et al (2026) Leather waste into functional materials: composite nanoarchitectonics, energy systems, and environmental applications. Int J Energy Water Resour 10:2. https://doi.org/10.1007/s42108-025-00433-0
41. Pasos-Panqueva J, Baker A, Camargo-Valero MA (2024) Unravelling the impact of light, temperature and nutrient dynamics on duckweed growth: a meta-analysis study. J Environ Manage 366:121721. https://doi.org/10.1016/j.jenvman.2024.121721
42. Imron MF, Kurniawan SB, Soegianto A, Wahyudianto FE (2019) Phytoremediation of methylene blue using duckweed (*Lemna minor*). Heliyon 5:e02206. https://doi.org/10.1016/j.heliyon.2019.e02206
43. Can-Terzi B, Goren AY, Okten HE, Sofuoglu SC (2021) Biosorption of methylene blue from water by live *Lemna minor*. Environ Technol Innov 22:101432. https://doi.org/10.1016/j.eti.2021.101432
44. Reema RM, Saravanan P, Kumar MD, Renganathan S (2011) Accumulation of methylene blue dye by growing *Lemna minor*. Sep Sci Technol 46:1052–1058. https://doi.org/10.1080/01496395.2010.528503
45. Jeffrey KB, Zheng ALT, Hii TT et al (2024) Sustainable dye wastewater treatment: utilizing duckweed-derived adsorbents for efficient methylene blue removal. Biomass Convers Biorefinery. https://doi.org/10.1007/s13399-024-06432-1
46. Ofoedu CE, Bozkurt H, Mortimer JC (2025) Towards sustainable food security: exploring the potential of duckweed (Lemnaceae) in diversifying food systems. Trends Food Sci Technol 161:105073. https://doi.org/10.1016/j.tifs.2025.105073
47. Aragaw TA, Bogale FM, Aragaw BA (2021) Iron-based nanoparticles in wastewater treatment: a review on synthesis methods, applications, and removal mechanisms. J Saudi Chem Soc 25:101280. https://doi.org/10.1016/j.jscs.2021.101280
48. Keshta BE, Gemeay AH, Kumar Sinha D et al (2024) State of the art on the magnetic iron oxide nanoparticles: synthesis, functionalization, and applications in wastewater treatment. Results Chem 7:101388. https://doi.org/10.1016/j.rechem.2024.101388
49. Taşdemir A, Akman N, Akkaya A et al (2022) Green and cost-effective synthesis of zinc oxide thin films by L-ascorbic acid (AA) and their potential for electronics and antibacterial applications. Ceram Int 48:10164–10173. https://doi.org/10.1016/j.ceramint.2021.12.228
50. Roy D, Johnson HM, Hurlock MJ et al (2024) Exploring the complex chemistry and degradation of ascorbic acid in aqueous nanoparticle synthesis. Angew Chem Int Ed. https://doi.org/10.1002/anie.202412542
51. Nene AG, Takahashi M, Wakita K, Umeno M (2016) Size controlled synthesis of Fe_3O_4 nanoparticles by ascorbic acid mediated reduction of $Fe(acac)_3$ without using capping agent. J Nano Res 40:8–19. https://doi.org/10.4028/www.scientific.net/JNanoR.40.8
52. Ariyanto T, Pradana NY, Saif MHN et al (2024) Reusable adsorbent of magnetite in mesoporous carbon for antibiotic removal. Environ Sci Pollut Res 31:35824–35834. https://doi.org/10.1007/s11356-024-33658-3
53. Siddiqa A, Khatun MH, Mostafa MG (2025) Synthesis of magnetite-maghemite nanocomposite adsorbents coated with leaf extract for removal of lead ions from water. Desalin Water Treat 321:100979. https://doi.org/10.1016/j.dwt.2024.100979
54. Sood A, Arora V, Shah J et al (2016) Ascorbic acid-mediated synthesis and characterisation of iron oxide/gold core–shell nanoparticles. J Exp Nanosci 11:370–382. https://doi.org/10.1080/17458080.2015.1066514
55. Sreeja V, Jayaprabha KN, Joy PA (2015) Water-dispersible ascorbic-acid-coated magnetite nanoparticles for contrast enhancement in MRI. Appl Nanosci 5:435–441. https://doi.org/10.1007/s13204-014-0335-0
56. Mosoarca G, Vancea C, Popa S et al (2020) *Syringa vulgaris* leaves powder a novel low-cost adsorbent for methylene blue removal: isotherms, kinetics, thermodynamic and optimization by Taguchi method. Sci Rep 10:17676. https://doi.org/10.1038/s41598-020-74819-x
57. Tenno T, Rikmann E, Zekker I et al (2016) Modelling equilibrium distribution of carbonaceous ions and molecules in a heterogeneous system of CaCO 3 –water–gas. Proc Est Acad Sci 65:68. https://doi.org/10.3176/proc.2016.1.07
58. Zekker I, Rikmann E, Oja J et al (2023) The selective salinity and hydrazine parameters for the start-up of non-anammox-specific biomass SBR. Int J Environ Sci Technol 20:12597–12610. https://doi.org/10.1007/s13762-023-05055-9
59. Vikesland PJ, Rebodos RL, Bottero JY et al (2016) Aggregation and sedimentation of magnetite nanoparticle clusters. Environ Sci Nano 3:567–577. https://doi.org/10.1039/C5EN00155B
60. Zhang Z, Wang G, Li W et al (2021) Photocatalytic activity of magnetic nano-β-FeOOH/Fe3O4/biochar composites for the enhanced degradation of methyl orange under visible light. Nanomaterials 11:526. https://doi.org/10.3390/nano11020526
61. Zubair YO, Fuchida S, Tokoro C (2020) Insight into the mechanism of arsenic(III/V) uptake on mesoporous zerovalent iron–magnetite nanocomposites: adsorption and microscopic studies. ACS Appl Mater Interfaces 12:49755–49767. https://doi.org/10.1021/acsami.0c14088
62. Pastukhov AV (2021) Magnetic sorbents based on hypercross-linked copolymers of styrene and divinylbenzene with immobilized iron oxides. React Funct Polym 160:104823. https://doi.org/10.1016/j.reactfunctpolym.2021.104823
63. Alekseeva OV, Rodionova AN, Bagrovskaya NA, Agafonov AV (2016) Synthesis, structure, and properties of a bentonite–magnetite composite. Prot Met Phys Chem Surf 52:819–824. https://doi.org/10.1134/S2070205116050038
64. Hu J-D, Zevi Y, Kou X-M et al (2010) Effect of dissolved organic matter on the stability of magnetite nanoparticles under different pH and ionic strength conditions. Sci Total Environ 408:3477–3489. https://doi.org/10.1016/j.scitotenv.2010.03.033
65. Mørup S, Hansen MF, Frandsen C (2010) Magnetic interactions between nanoparticles. Beilstein J Nanotechnol 1:182–190. https://doi.org/10.3762/bjnano.1.22
66. Nedylakova M, Medinger J, Mirabello G, Lattuada M (2024) Iron oxide magnetic aggregates: aspects of synthesis, computational approaches and applications. Adv Colloid Interface Sci 323:103056. https://doi.org/10.1016/j.cis.2023.103056
67. Abbas M, Parvatheeswara Rao B, Naga SM et al (2013) Synthesis of high magnetization hydrophilic magnetite (Fe3O4) nanoparticles in single reaction—surfactantless polyol process. Ceram Int 39:7605–7611. https://doi.org/10.1016/j.ceramint.2013.03.015
68. Saiphaneendra B, Saxena T, Singh SA et al (2017) Synergistic effect of co-existence of hematite (α-Fe 2 O 3) and magnetite (Fe 3 O 4) nanoparticles on graphene sheet for dye adsorption. J

Environ Chem Eng 5:26–37. https://doi.org/10.1016/j.jece.2016.11.017
69. Sato J, Kobayashi M, Kato H et al (2014) Hydrothermal synthesis of magnetite particles with uncommon crystal facets. J Asian Ceram Soc 2:258–262. https://doi.org/10.1016/j.jascer.2014.05.008
70. Culita DC, Patron L, Oprea O et al (2013) Detailed characterization of functionalized magnetite and ascertained effects. J Nanopart Res 15:1916. https://doi.org/10.1007/s11051-013-1916-7
71. Hossain MD, Zhang Q, Cheng T et al (2021) Graphitization of low-density amorphous carbon for electrocatalysis electrodes from ReaxFF reactive dynamics. Carbon N Y 183:940–947. https://doi.org/10.1016/j.carbon.2021.07.080
72. Ribeiro VGP, Barreto ACH, Denardin JC et al (2013) Magnetic nanoparticles coated with anacardic acid derived from cashew nut shell liquid. J Mater Sci 48:7875–7882. https://doi.org/10.1007/s10853-013-7477-4
73. Xu Y, Sherwood J, Qin Y et al (2015) A general approach to the synthesis and detailed characterization of magnetic ferrite nanocubes. Nanoscale 7:12641–12649. https://doi.org/10.1039/C5NR03096J
74. Zheng ALT, Boonyuen S, Ohno T, Andou Y (2021) Accessing effects of aliphatic dicarboxylic acid towards the physical and chemical changes in low temperature hydrothermally reduced graphene hydrogel. J Porous Mater 28:1291–1300. https://doi.org/10.1007/s10934-021-01072-6
75. Zheng ALT, Boonyuen S, Li GY et al (2021) Design of reduced graphene hydrogel with alkylamine surface functionalization through immersion/agitation method and its adsorption mechanism. J Mol Struct 1245:131008. https://doi.org/10.1016/j.molstruc.2021.131008
76. Baek G, Saeed M, Choi H-K (2021) Duckweeds: their utilization, metabolites and cultivation. Appl Biol Chem 64:73. https://doi.org/10.1186/s13765-021-00644-z
77. Bagbi Y, Yomgam P, Libang E et al (2024) Waste bamboo-derived magnetically separable bamboo-activated carbon: from characterization to effective remediation of fluoride (F−) ions from water. RSC Adv 14:24952–24968. https://doi.org/10.1039/D4RA03752A
78. Tenea A-G, Dinu C, Rus PA et al (2024) Exploring adsorption dynamics of heavy metals onto varied commercial microplastic substrates: isothermal models and kinetics analysis. Heliyon 10:e35364. https://doi.org/10.1016/j.heliyon.2024.e35364
79. Sahu S, Pahi S, Sahu JK et al (2020) Kendu (*Diospyros melanoxylon* Roxb) fruit peel activated carbon—an efficient bioadsorbent for methylene blue dye: equilibrium, kinetic, and thermodynamic study. Environ Sci Pollut Res 27:22579–22592. https://doi.org/10.1007/s11356-020-08561-2
80. Ji B, Zhu L, Song H et al (2019) Adsorption of methylene blue onto novel biochars prepared from *Magnolia grandiflora* Linn fallen leaves at three pyrolysis temperatures. Water Air Soil Pollut 230:281. https://doi.org/10.1007/s11270-019-4330-7
81. Wei F, Jin S, Yao C et al (2023) Revealing the combined effect of active sites and intra-particle diffusion on adsorption mechanism of methylene blue on activated red-pulp pomelo peel biochar. Molecules 28:4426. https://doi.org/10.3390/molecules28114426
82. Ceretta MB, Nercessian D, Wolski EA (2021) Current trends on role of biological treatment in integrated treatment technologies of textile wastewater. Front Microbiol. https://doi.org/10.3389/fmicb.2021.651025
83. Yang X, Wan Y, Zheng Y et al (2019) Surface functional groups of carbon-based adsorbents and their roles in the removal of heavy metals from aqueous solutions: a critical review. Chem Eng J 366:608–621. https://doi.org/10.1016/j.cej.2019.02.119
84. Martinez S, Stern I (2002) Thermodynamic characterization of metal dissolution and inhibitor adsorption processes in the low carbon steel/mimosa tannin/sulfuric acid system. Appl Surf Sci 199:83–89. https://doi.org/10.1016/S0169-4332(02)00546-9
85. Ebisike K, Elvis Okoronkwo A, Kanayo Alaneme K, Jeremiah Akinribide O (2023) Thermodynamic study of the adsorption of Cd2+and Ni2+onto chitosan – Silica hybrid aerogel from aqueous solution. Results Chem 5:100730. https://doi.org/10.1016/j.rechem.2022.100730
86. Mehmandost N, Goudarzi N, Arab Chamjangali M, Bagherian G (2022) Removal of methylene blue and crystal violet in binary aqueous solution by magnetic terminalia catappa kernel shell biosorbent using box–behnken design. J Iran Chem Soc 19:3769–3781. https://doi.org/10.1007/s13738-022-02552-5
87. Dominguez M, Mendoza J, Figueroa K (2024) Adsorption of methylene blue dye using common walnut shell (*Juglans regia*) like biosorbent: implications for wastewater treatment. Green Chem Lett Rev 17. https://doi.org/10.1080/17518253.2024.2362257
88. Balarak D, Baniasadi M, Lee S-M, Shim MJ (2021) Ciprofloxacin adsorption onto *Azolla filiculoides* activated carbon from aqueous solutions. Desalin Water Treat 218:444–453. https://doi.org/10.5004/dwt.2021.26986
89. Kokalj A (2023) On the use of the Langmuir and other adsorption isotherms in corrosion inhibition. Corros Sci 217:111112. https://doi.org/10.1016/j.corsci.2023.111112
90. Shi Y, Zhang T, Chang Q et al (2023) Performance stability and regeneration property of catalytic membranes coupled with advanced oxidation process: a comprehensive review. Sustainability 15:7556. https://doi.org/10.3390/su15097556
91. Razali SZ, Aziz MY, Edinur HA, Razali Ishak A (2020) Adsorption of methylene blue onto iron oxide magnetic nanoparticles coated with sugarcane Bagasse. IOP Conf Ser Earth Environ Sci 596:012052. https://doi.org/10.1088/1755-1315/596/1/012052
92. Tripathy S, Sahu S, Patel RK et al (2022) Novel Fe_3O_4-modified biochar derived from Citrus Bergamia peel: a green synthesis approach for adsorptive removal of methylene blue. ChemistrySelect. https://doi.org/10.1002/slct.202103595
93. Lee E-J, Lee J-W (2024) Synergistic effect of adsorption and photolysis on methylene blue removal by magnetic biochar derived from lignocellulosic biomass. Bioresour Technol 407:131124. https://doi.org/10.1016/j.biortech.2024.131124
94. Yao X, Ji L, Guo J et al (2020) Magnetic activated biochar nanocomposites derived from wakame and its application in methylene blue adsorption. Bioresour Technol 302:122842. https://doi.org/10.1016/j.biortech.2020.122842
95. Chen D, Chen J, Hu Z et al (2021) One-step synthesis of magnetic biosorbent for the removal of methylene blue. Desalin Water Treat 233:341–350. https://doi.org/10.5004/dwt.2021.27523
96. Li C, Wang X, Meng D, Zhou L (2018) Facile synthesis of low-cost magnetic biosorbent from peach gum polysaccharide for selective and efficient removal of cationic dyes. Int J Biol Macromol 107:1871–1878. https://doi.org/10.1016/j.ijbiomac.2017.10.058
97. El-Kalliny AS, Abdel-Wahed MS, Abdel-Hady NA et al (2024) Rapid adsorption of cationic dyes on a novel magnetic biosorbent manganese ferrite (MnFe2O4) encapsulated in *Scenedesmus obliquus*. Sep Purif Technol 330:125497. https://doi.org/10.1016/j.seppur.2023.125497
98. Mu Y, Du H, He W, Ma H (2022) Functionalized mesoporous magnetic biochar for methylene blue removal: performance assessment and mechanism exploration. Diamond Relat Mater 121:108795. https://doi.org/10.1016/j.diamond.2021.108795
99. Özer A, Toprak M (2023) Highly efficient removal of methylene blue from aqueous solution by magnetic biochar prepared from

hawthorn seeds. Environ Prog Sustain Energy. https://doi.org/10.1002/ep.14127

100. Pandey A, Bhagat A, Bhaduri B (2025) Magnetite nanoparticles loaded onto inexpensive candle soot particles as a promising material for the elimination of potentially toxic aqueous methylene blue and crystal violet dye molecules. J Environ Chem Eng 13:116024. https://doi.org/10.1016/j.jece.2025.116024
101. Mortada WI, Ghaith MM, Khedr NE et al (2024) Mesoporous magnetic biochar derived from common reed (*Phragmites australis*) for rapid and efficient removal of methylene blue from aqueous media. Environ Sci Pollut Res 31:42330–42341. https://doi.org/10.1007/s11356-024-33860-3
102. Mishra A, Pandey J, Ojha H et al (2024) A green and economic approach to synthesize magnetic *Lagenaria siceraria* biochar (γ-Fe2O3-LSB) for methylene blue removal from aqueous solution. Environ Sci Pollut Res 31:34038–34055. https://doi.org/10.1007/s11356-024-33477-6
103. Chistie SM, Naik SU, Rajendra P et al (2025) Production and characterization of magnetic Biochar derived from pyrolysis of waste Areca nut husk for removal of methylene blue dye from wastewater. Sci Rep 15:23209. https://doi.org/10.1038/s41598-025-03359-z
104. Mishra A, Kaur L, Sharma M et al (2025) Magnetic biochar from marigold floral waste: synthesis, characterization, and adsorptive removal of methylene blue. J Mol Struct 1341:142657. https://doi.org/10.1016/j.molstruc.2025.142657
105. Saeed A, Sharif M, Iqbal M (2010) Application potential of grapefruit peel as dye sorbent: kinetics, equilibrium and mechanism of crystal violet adsorption. J Hazard Mater 179:564–572. https://doi.org/10.1016/j.jhazmat.2010.03.041
106. Zhang L-L, Zaoui A, Sekkal W, Zheng Y-Y (2023) Interlayer adsorption of cationic dye on cationic surfactant-modified and unmodified montmorillonite. J Hazard Mater 442:130107. https://doi.org/10.1016/j.jhazmat.2022.130107
107. Saleh IM, Qasem HAM KMA, et al (2020) Efficient and selective adsorption and separation of methylene blue (MB) from mixture of dyes in aqueous environment employing a Cu(II) based metal organic framework. Inorganica Chim Acta 511:119787. https://doi.org/10.1016/j.ica.2020.119787
108. Ayad MM, El-Nasr AA (2010) Adsorption of cationic dye (Methylene Blue) from water using polyaniline nanotubes base. J Phys Chem C 114:14377–14383. https://doi.org/10.1021/jp103780w
109. Dabagh A, EL-Habacha M, Assouani A et al (2025) Remediation of hazardous dyes on low-cost biosorbent: batch and dynamic adsorption, phytotoxicity assessment, and application of industrial wastewater. Biomass Convers Biorefin. https://doi.org/10.1007/s13399-025-06531-7
110. Dabagh A, Assouani A, Zahra Erraji F et al (2024) Enhanced cationic/anionic dyes removal in wastewater by green nanocomposites synthesized from acid-modified biomass and CuFe2O4 nanoparticles: Mechanism, Taguchi optimization and toxicity evaluation. Environ Nanotechnol Monit Manag 22:101019. https://doi.org/10.1016/j.enmm.2024.101019
111. Bataineh SMB, Arafa IM, Abu-Zreg SM et al (2024) Synergistic effect of magnetic iron oxide nanoparticles with medicinal plant extracts against resistant bacterial strains. Magnetochemistry 10:49. https://doi.org/10.3390/magnetochemistry10070049
112. Wypij M, Jędrzejewski T, Trzcińska-Wencel J et al (2021) Green synthesized silver nanoparticles: antibacterial and anticancer activities, biocompatibility, and analyses of surface-attached proteins. Front Microbiol. https://doi.org/10.3389/fmicb.2021.632505
113. Menazea AA, Ismail AM, Samy A (2021) Novel green synthesis of zinc oxide nanoparticles using orange waste and its thermal and antibacterial activity. J Inorg Organomet Polym Mater 31:4250–4259. https://doi.org/10.1007/s10904-021-02074-2
114. Lih TK, Zheng ALT, Tan HY et al (2025) Low intensity UV driven dual functional Cu doped BiVO4 for enhanced methylene blue degradation and *Staphylococcus aureus* inactivation. Sci Rep 15:34568. https://doi.org/10.1038/s41598-025-17994-z
115. Manivel CM, Zheng ALT, Kannan R et al (2025) ZIF-8/graphene composite for photocatalytic degradation under low intensity UV irradiation and antibacterial applications. Sci Rep 15:33875. https://doi.org/10.1038/s41598-025-07444-1
116. Maran MA, Zheng ALT, Tan HY et al (2025) Assessing the photocatalytic performance of hydrothermally synthesized Fe-Doped BiVO4 under Low-Intensity UV irradiation. Arab J Sci Eng. https://doi.org/10.1007/s13369-025-10278-8